

ABSTRACT

BAILEY, TIFFANI NICOLE. Tailored Surfaces: Modifying Chemical and Physical Properties at the Liquid/Solid Interface to Address Optimizing Surface Chemistry Applications. (Under the guidance of Dr. Chris Gorman and Dr. Jan Genzer.)

The research presented in this PhD thesis focuses on surface modification techniques to enhance potentially useful behavior of materials on surfaces. The principal objectives of this work include (1) investigating the physico-chemical phenomena at the liquid/substrate interface to enhance current methods of moving meso- scale liquid droplets (2) developing a polymer brush gradient on silicon to enhance the efficiency in binding and detection of probe molecules and (3) tailoring a poled substrate by electrostatically binding polar molecules to form a molecular assembly. Research was conducted by varying the physical properties of a liquid in motion (including, surface tension, viscosity) and the characteristics of the substrate upon which the liquid moves. The latter will include both physical and “chemical” roughness (i.e., variation of chemical functionalities present at the surface unit) of the substrate.

We also identified an efficient method of increasing DNA immobilization and hybridization. A polymer brush molecular weight gradient was used as a platform for DNA attachment. Fluorescence microscopy was used to obtain relative fluorescence intensity values indicating DNA hybridization and attachment to the polymer backbone. The microscopy technique provided evidence indicating an increase in DNA attachment to the polymer backbone as the polymer chain length increased.

A method of using self-assembly to develop interactions between a polarized ferroelectric domain and polar molecules was also studied. We demonstrated selective binding of

bromoacetic acid to a single faced poled lithium niobate surface using XPS. Thus, a poled substrate was tailored by electrostatically binding polar molecules to form a molecular assembly.

Tailored Surfaces: Modifying Chemical and Physical Properties at the Liquid/ Solid Interface
to Address Optimizing Surface Chemistry Applications

by

Tiffani Nicole Bailey

A dissertation submitted to the Graduate Faculty of

North Carolina State University

In partial fulfillment of the

Requirements for the degree of

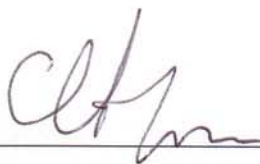
Doctor of Philosophy

Chemistry

Raleigh, NC

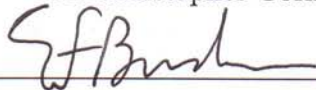
December 15, 2006

Approved by:

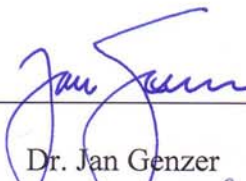


Dr. Christopher Gorman

(Co-Chair)

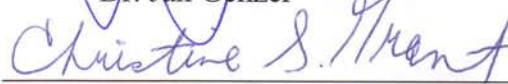


Dr. Edmond Bowden



Dr. Jan Genzer

(Co-Chair)



Dr. Christine Grant

DEDICATION

This thesis is dedicated to my parents, Professor Ronnie and Mrs. Terry Bailey.

Thank you for always making me feel like there was no limit to anything I ever wanted to achieve. I could not have done this without you.

BIOGRAPHY

Tiffani Nicole Bailey was born in Portsmouth, VA on May 16, 1980 to Ronnie and Terry Bailey. At the age of 1, she and her family moved to the place she considers home in Greensboro, NC. Tiffani has one younger brother, Ronnie Terence Bailey. Tiffani graduated from Dudley Math, Science and Technology Academy in 1998. She attended Hampton University in Hampton, VA to pursue a degree in Chemistry. As an undergraduate, Tiffani was a member of the American Chemical Society, American Society for Pharmacology and Experimental Therapeutics, Beta Kappa Chi National Scientific Honor Society, Delta Sigma Theta Sorority, Inc and the Student Government Association. She was also the recipient of awards from the Office of Naval Research, Virginia Air and Space Grant Consortium, National Science Foundation, and the National Organization for the Advancement of Black Chemists and Chemical Engineers. The author studied abroad in places such as: Oxford University in Oxford, England at the Edgerton University in Kenya, Africa. In 1998, she graduated with honors from Hampton University with a Bachelors of Science in Chemistry. In the fall of 2002, Tiffani started her graduate career in Chemistry at North Carolina State University located in Raleigh, North Carolina. Under the guidance of Dr. Chris Gorman and Dr. Jan Genzer, Tiffani conducted inter-disciplinary research focused on tailoring surfaces by modifying their chemical and physical properties for novel surface chemistry applications.

ACKNOWLEDGMENTS

First and foremost in the words of K.K. Wong “ I would like to thank God for giving the scientific community such wonderful insights into His creation.” I am grateful for having the opportunity to be used as a vessel.

I would like to thank my advisors Dr. Chris Gorman and Dr. Jan Genzer (Dr.G). Dr. Gorman, I am pleased to have had the chance to work under your leadership. I have learned how to conduct research, analyze the data, and most of all “make my research tell a story”. Your words of wisdom have helped me become a better chemist. Thank you for your support and guidance. Dr.G, even though I am not a chemical engineer you welcomed me into your group 4 years ago without any hesitation. You have been more than just a boss but a person whom I truly admire as a scientist, professor, and mentor. Thank you for the leadership and the laughs. In addition to my advisors, I would also like to thank all of the past and present members of the Gorman and Genzer groups for your support and assistance.

To my committee members Dr. Ed Bowden and Dr. Christine Grant, I thank you for your assistance and for challenging my abilities to become a better scientist. Dr. Grant words cannot express how thankful I am to have come across your path. Thank you for everything. I would also like to acknowledge the encouragement and support from Dr. Dave Shafer the Assistant Dean of the Graduate School.

Throughout the years, several programs and mentors have exposed me to the wonderful world of science. I am overly grateful to Dr. Patricia Legrand, Mrs. Toni

Lamberth, Dr. Henry Collins, and Dr. Valarie Guthrie, who have supported and encouraged me to pursue a degree in Chemistry because of their own love for the field. Programs such as the NC A&T Saturday Academy, Greensboro Area Math and Science & Education Center Programs, NC A&T Engineers Starter Program, Bennett College Pre-College Program, Florida A & M University Actuarial Science Program and the Ronald E. McNair Program were very instrumental in exposing me to the S.T.E.M. (Science, Technology, Engineering, and Mathematics) disciplines and keeping me in the “pipeline” since the age of 7 years old. While at Hampton University, I had the pleasure of crossing paths of the following instrumental chemistry professors, Dr. Isai Urasa, Dr. Willie Darby, and Drs. Edmond and Grace Ndip, Dr. Ward Mavura and Dr. Joseph Williams.

A special thanks to Tashni-Ann Coote and Ibrahim Bori, friends and colleagues who kept me motivated and determined that we would all would see the finish line in the end. Thank you Shani Smith, Michelle Bowman, and Courtney Hinson for your support during my years as a graduate student.

Finally, I would like to thank my family for believing in me. I have always remembered the saying “Every river has its source”. Thank you for being my source as I traveled this journey. Congratulations little brother, it looks like we will be graduating together, I am proud of you. To my future husband, William G. Lash your words of encouragement, patience and flowers made me feel that I was never alone. You are everything that I dreamed of in a partner for life. Thank you.

TABLE OF CONTENTS

List of Tables.....	viii
List of Figures.....	xii
List of Schemes.....	xiii

Chapter 1: General Introduction and Project Objectives..... 1

1.1	Meso-scale Liquid Transport via Surface Tension Gradient	
	1.1.1: Surface Wettability and Modifications.....	1
	1.1.2: Motion of Liquid on a Chemical gradient	7
1.2	Surface Modifications: Surface Tethered Polymers	
	1.2.1 Polymer Thin Films.....	9
	1.2.2 Surface Based Polymerization.....	10
1.3	Surface Modification: Charge Modification	
	1.3.1 Polled Lithium Niobate.....	11
1.4	References.....	13

Chapter 2: Liquid Transport: Modification of Surface Topography to Reduce Friction at the Liquid/Substrate Interface

2.1	Project Goals and Motivation.....	15
2.2	Introduction.....	15
2.3	Results and Discussion.....	19
2.4	Conclusions.....	24
2.5	Implementation / Experimental	
	2.5.1 Preparation of Porous Silicon.....	25
	2.5.2 Preparation of F8H2 Gradient on Porous and Flat Surface....	26
	2.5.3 Characterization of the Porous Silicon Surface.....	27
	2.5.4 Measurement of Contact Angles and Drop Velocity.....	27
2.6	References.....	29

Chapter 3: Liquid Transport: Effects of Surface Tension and Viscosity on a Viscous Droplet in Motion

3.1	Project Goals and Motivation.....	31
3.2	Introduction	
	3.2.1 Mechanisms to Induce Droplet Motion.....	32
	3.2.2 Droplet Contact Line Dynamics and Composition.....	34
3.3	Results and Discussion	
	3.3.1 Viscous Drop Motion on a Tilted Non-Wettable Solid and Chemical Gradient.....	36
3.4	Conclusions.....	48
3.5	Implementation / Experimental	

	3.5.1 Surface Preparation.....	49
	3.5.2 Contact Angle Measurements.....	49
	3.5.3 Measurements of Drop Velocities and Sizes.....	50
	3.5.4 Equipment.....	51
3.6	References.....	52
Chapter 4:	Tailored Surfaces: Polymer Brush Gradients Synthesized via ATRP as a Platform for DNA Immobilization	
4.1	Project Goals and Motivation.....	54
4.2	Introduction.....	56
4.3	Results and Discussion	
	4.3.1 Surface Modification and Characterization.....	58
4.4	Conclusions.....	71
4.5	Implementation / Experimental	
	4.5.1 Materials.....	72
	4.5.2 ATRP Synthesis of a Surface Initiated Polymerization Gradient.....	72
	4.5.3 Covalent coupling via 1,1'-carbonyldiimidazole (CDI) reaction.....	74
	4.5.4 Capture Probe Immobilization and DNA Hybridization.....	74
	4.5.5 Instrumentation.....	75
4.6	References.....	77
Chapter 5:	Controllable Nano Patterned Polar Surfaces for Molecular Pattern Formation and Transfer	
5.1	Project Goals and Motivation.....	79
5.2	Introduction	
	5.2.1 Ferroelectric Materials.....	80
	5.2.2 Self Assembly of Polar Materials.....	82
5.3	Results and Discussion	
	5.3.1 Single Faced Poled Lithium Niobate.....	83
	5.3.2 Periodic Poled Lithium Niobate.....	88
5.4	Conclusions.....	92
5.5	Experimental	
	5.5.1 Materials.....	93
	5.5.2 Surface Passivation.....	93
	5.5.3 Instrumentation.....	94
5.6	References.....	95
Chapter 6:	Summary and Outlook	
6.1	Systematic Study of Pore Size for Water Motion on Wettability Gradients.....	97
6.2	Movement of liquids containing suspended particles.....	98
6.3	Systematic study on the Weight Capacity of DNA in a Polymer Brush.....	99
6.4	Polarization Driven Self Assembly using Polar Silanes.....	99

LIST OF FIGURES

Figure 1.1	Illustration of a droplet in contact with air and a solid substrate.....	2
Figure 1.2	Simplified schematic showing general formation of a self-assembled monolayer.....	4
Figure 1.3	Illustration of the diffusion source molecules to the silica/silicon wafer from a molecular gradient.....	5
Figure 1.4	Illustration of two types of polymer film formation: grafting onto, and grafting from.....	9
Figure 2.1	(a) Cross sectional scanning electron microscopy image of porous silicon. The diagram depicts the outline of the porous region after etching. (b) Relative fluorine concentration on the porous substrate decorated with the gradient in F8H2 self-assembled monolayer as determined from the combinatorial near-edge x-ray absorption fine structure spectroscopy experiments.....	20
Figure 2.2	Advancing (solid symbols) and receding (open symbols) contact angles of deionized water as a function of the position on the F8H2 molecular gradient created on top of a flat (a) and porous (b) silicon substrate. The volume of the probing liquid was 4 (■), 6 (●), 8 (▲), 10 (▼), and 12 (◆) μl.....	21
Figure 2.3	Capillary number ($Ca=v/v^*$) as a function of the normalized drop radius ($R^*=R \cdot \partial \cos(\theta) / \partial x$) associated with motion of a droplet of deionized water along the F8H2 molecular gradient created on top of a flat (open symbols) and porous (solid symbols) silicon substrate. During the course of the experiment the drop velocity was collected at multiple positions on the sample. The data presented in Figure 3 have been compiled from the drop velocity data collected at the constant contact angle of water equal to: 70° (▽), 65° (△), 60° (◇), 100° (■), and 80° (●). The lines are meant to guide the eye.....	23
Figure 3.1	Diagram represents competing forces acting on a drop: weight or gravitational forces(A) and capillary forces (B).The weight of the drop is responsible for a downward pull of the droplet, while the capillary forces affect the internal flow within the droplet.....	35

Figure 3.2	Image depicts a 30 μ L ethylene glycol droplet moving across a fluorinated gradient on Si. A trail is left behind as the droplet traverses the gradient substrate.....	37
Figure 3.3	Graph depicting variations in surface tension (\blacktriangle) and viscosity (\blacksquare) for aqueous solutions containing various weight percentages of sucrose at 25 $^{\circ}$ C. Both an increase in surface tension and viscosity are shown as the sucrose concentration is increased.....	38
Figure 3.4	A graph depicting the relationship between the volume of H ₂ O droplets (3, 5, 10, 15, and 30 μ L) and the tilt angle of a fluorinated homogeneous monolayer on Si substrate required to move them. The graph shows the tilt angle required to induce motion was achieved at 15 μ L and 30 μ L.....	40
Figure 3.5:	The advancing (\bullet) and receding (\blacksquare) positions of droplets containing varying sucrose concentrations plotted as a function of time. The sucrose concentrations are (A) 0 %, (B) 10 wt %, (C) 20 wt % and (D) 60 wt %, respectively.....	42
Figure 3.6:	Graph of droplet velocity vs. time for droplets in motion on a 60 $^{\circ}$ tilted substrate. The insert shows a photograph of a 20-wt % sucrose droplet in motion. Droplets contained (\blacklozenge) 0 wt %, (\blacksquare) 10 wt %, (\blacktriangle) 20 wt % and (\times) 60 wt % sucrose in water. Lines are drawn through the symbols merely as a guide to the eye. Velocity is measured immediately at the onsite of motion during liquid/ substrate interaction.....	43
Figure 3.7:	Graph of droplet velocity vs. time graph for droplets in motion on an F8H2 gradient. Droplets contained (\blacklozenge) 0 wt %, (\blacksquare) 10 wt %, (\times) 22wt %, (\bullet) 36 wt % and (\blacktriangle) 42 wt % sucrose in water. Faster motion for the 22 wt% solution resulted in collection of fewer points. Lines are drawn through the symbols merely as a guide to the eye.....	44
Figure 3.8:	Graph of velocity vs viscosity on a 60 $^{\circ}$ tilted substrate. 30uL droplets of 0, 10, 22, 36, 42, 50, 58 and 60wt% of sucrose were used.....	45
Figure 3.9:	Depicts Ca vs Bo $_{\alpha}$ of 30uL droplets moving on varying inclination angles (20,40and 60 $^{\circ}$).....	47
Figure 3.10:	Depicts an angle tilt apparatus. The figures include dimensions and set up...51	
Figure 4.1:	Provides the dry thickness polymer brush profile using ellipsometry across a silicon substrate corresponding to position and time.....	60

Figure 4.2:	FT-IR spectra of hydroxy stretching region plotted as a function of time. Hydroxyl groups were monitored for pHEMA (a), pHEMA/CDI 2hrs (b), pHEMA/CDI 6hrs (c) and pHEMA/CDI 27hrs (d)...	62
Figure 4.4:	FTIR spectra of a pHEMA brush attached to a Si substrate before and after reaction with fluoresceinamine.....	64
Figure 4.5:	Graph showing fluorescence intensity vs dry pHEMA thickness plot for fluoresceinamine attachment to a functionalized pHEMA gradient.....	65
Figure 4.6:	Fluorescence micrographs (top) and corresponding intensity depicts a.unreacted pHEMA and b-d pHEMA after grafting with DNA probe and complimentary strand via CDI coupling for 63.5 (nm), 37.0 (nm), 21.3 (nm).....	68
Figure 4.7:	Graph shows fluorescence intensity vs polymer thickness data for hybridization of complimentary (■) and non-complimentary (▲) DNA on target DNA modified polymer gradient. The single data point at zero. Dry pHEMA thickness indicates the Background for both samples.....	69
Figure 4.8:	Atomic force microscopy images DNA coated Gold nanoparticles in a low (22-38nm) and high molecular weight polymer brush (62-74nm). In the low molecular weight regime the density of particles is $18.205 \mu\text{m}^3$ vs that of the high molecular weight regime of $7.843\mu\text{m}^3$	71
Figure 4.9:	Illustrates the apparatus designed to systematically vary molecular weight and or grafting density on a substrate.....	73
Figure 5.1:	Illustration is shown of the domain directions of a periodically poled lithium niobate. The E_{app} arrow indicates the direction in which the electric field is applied.....	81
Figure 5.2:	X-ray photoelectron spectra at a takeoff angle of 90° of poled lithium niobate positively and negatively charged surfaces after vapor phase exposure to bromo acetic acid ($\text{Br}_2\text{CH}_2\text{CO}_2\text{H}$). Representative peaks of Nb and Br are indicated. The $\text{Br}_2\text{CH}_2\text{CO}_2\text{H}$ self assembled monolayer was formed under the following conditions (temperature 120°C , vapor pressure 60 torr for 1hr). The Br/Nb (+) / Br/Nb (-) intensity ratio was 3.9 to 1.....	85
Figure 5.3:	X-ray photoelectron spectra at a takeoff angle of 90° of poled lithium niobate positively and negatively charged surfaces after vapor phase exposure to bromo acetic acid ($\text{Br}_2\text{CH}_2\text{CO}_2\text{H}$). Representative peaks	

	of Nb and Br are indicated. The Br/Nb (+) / Br/Nb (-) intensity ratio was .749/.45.....	86
Figure 5.4:	X-ray photoelectron spectra at a takeoff angle of 90° of poled lithium niobate positively and negatively charged surfaces after vapor phase exposure to bromo acetic acid (Br ₂ CH ₂ CO ₂ H). Representative peaks of Nb and Br are indicated. The Br ₂ CH ₂ CO ₂ H self assembled monolayer was formed under the following conditions(temperature 100°C, vapor pressure 105 torr for 1 hr). The Br/Nb (+) / Br/Nb (-) intensity ratio was .295/.137.....	87
Figure 5.5:	Diagram of periodic poled LiNbO ₃ as purchased. Illustration (left) indicates the spacing and charge between each periodically poled domain. The right illustration provides the aerial view of the entire periodically poled sample on a single lithium niobate surface.....	88
Figure 5.6:	TOF-SIMS images of a. Br, b. CH, c. H, d. OH (negative).....	90
Figure 5.7:	TOF-SIMS images of a. H, b. Br, c. OH, d. C (negative).....	91
Figure 5.8:	TOF-SIMS images of a. Br, b. total scan (positive).....	92

LIST OF TABLES

Table 3.5.1:	Contact angle measurements ($^{\circ}$) of deionized water, sucrose and glucose.....	50
Table 4.1.	List of DNA sequences.....	66

LIST OF SCHEMES

Scheme 4.1:	Schematic illustration of oligonucleotide attachment via carbonyldiimidazole coupling to surface anchored polymer. DP represents DNA capture probe. DC represents the complimentary strand to DP with a fluorophore attachment.....	55
Scheme 4.2:	Depicts the synthetic route to forming poly(hydroxyethylmethacrylate).....	59
Scheme 4.3:	Schematic formation of carbonyldiimidazole attachment to the polymer brush backbone.....	63
Scheme 5.1:	Illustration of the process used to create electrostatic interaction between bromoacetic acid and lithium niobate.....	83

Chapter 1: General Introduction and Project Objective:

The work presented in this PhD dissertation is centered on surface modification techniques used to enhance potentially useful behavior of material on surfaces. The topics discussed include liquid transport on a surface and surface tethered polymers used for DNA binding. This dissertation will also explore the possibility of selective binding of polar molecules to polarized, ferroelectric surfaces as a new motif for self-assembly. These three areas of research are each unified by a simple concept: tailoring the surface to optimize behaviors in surface chemistry applications.

1.1: Meso-scale Droplet Motion Via Surface Tension Gradient

1.1.1: Surface Wettability and Modifications

Wetting is among the many properties of a surface that can be tailored for a specific application¹ The wettability of a surface by a liquid is defined by the point of contact between a droplet on a horizontal surface. The spreading parameter of a liquid on a substrate (S) relates to the wettability of the substrate and the wettability of the substrate by the liquid is related to the interfacial energies (γ) at the interfaces between the solid(s), liquid (l) and air (v) interface (1) as given by equation 1 below.¹

$$S = \gamma_{sv} - (\gamma_{sl} + \gamma_{lv}) \quad (1)$$

When $S > 0$, the liquid completely wets the surface. For $S < 0$, partial wetting occurs, during which the liquid forms a spherical cap on the surface.² In addition, upon partial wetting a

distinct droplet shape is produced which can be defined by the contact angle that the droplet makes at three-phase boundary between the solid, liquid and vapor (Figure 1.1)

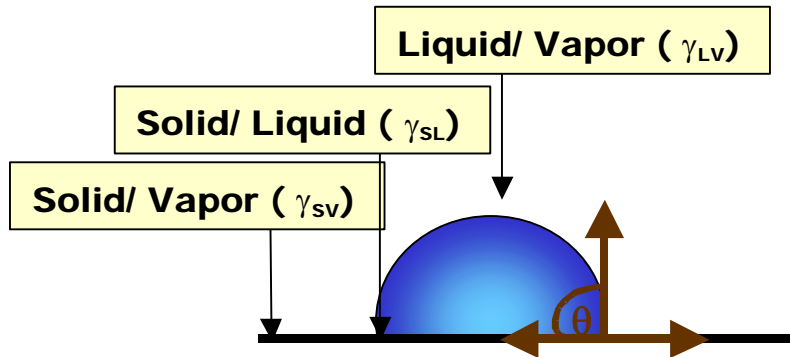


Figure 1.1: Illustration of a droplet in contact with an air and a solid substrate. Θ represents a static contact angle.

Young's equation correlates the surface tensions at the solid –liquid (γ_{sl}), solid-vapor (γ_{sv}), and liquid-vapor (γ_{lv}) phase to the equilibrium contact angle (θ_e) (2).

$$\cos\theta_e = \frac{\gamma_{sv} - \gamma_{sl}}{\gamma_{lv}} \quad (2)$$

This equilibrium contact angle assumes a flat, defect-free, non-reconstructing surface. Most “real” surfaces have chemical or physical defects or a combination of both. In order to assess the defects in terms of contact angle, the difference between the advancing and receding contact angles is considered.^{3,4} The advancing contact angle (θ_a) is measured by inflating the droplet until its contact angle stops changing as more volume is dispensed upon the surface.

Conversely, removing liquid from the droplet and measuring the contact angle provides the receding value (θ_r). The difference between the advancing and receding contact angles is called the contact angle hysteresis (CAH). CAH is thus a measure of the “ideality” of the surface. “Perfect surfaces” have $CAH \approx 0$. In contrast, large positive CAH values (the advancing CA is always higher than the receding (CA) indicate that the surface contains some physical or/and chemical heterogeneity.⁴

There have been several demonstrations that illustrate how surface wettability can be modified by changing the chemical and/or physical composition of the surface.^{5,6} One commonly used method of tailoring the surface properties is based on deposition of self-assembled monolayers (SAMs). SAMs are composed of molecules that spontaneously chemisorb and organize into an organized close-packed assembly on a substrate. Common substrates and reactants for the preparation of SAMs are noble metals (for attaching alkanethiols), hydrogen terminated surfaces (for attaching alkenes), and surfaces containing a metal oxide (for attaching organosilanes and alkylphosphonates).¹⁰ Figure 1.2 illustrates a self-assembling molecule, which includes an anchoring group with a strong preferential adsorption to the substrate, an alkyl chain and a terminal functionality (head group).

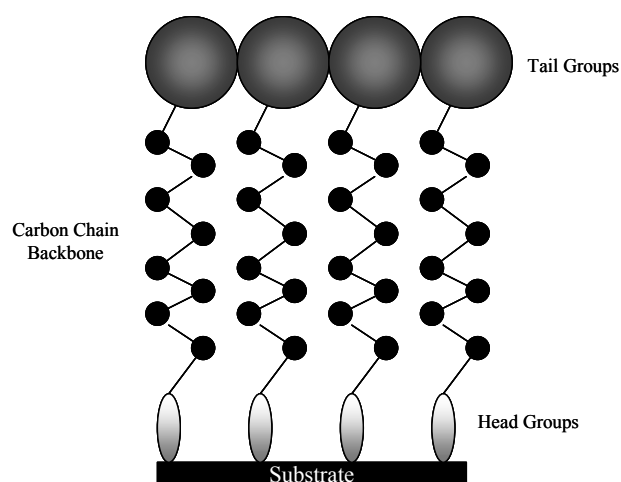


Figure 1.2: Simplified schematic showing the general formation of a self-assembled monolayer

The organization of the self-assembling molecules in SAMs is governed by the interplay between the packing of the molecules on the substrate, the interaction of the molecular head groups with the substrate and any interactions between the molecular terminal groups both with each other and with any liquids or vapors in contact with the SAM-modified surface.

Alkanethiol molecules are commonly used in the fabrication of a self-assembled monolayer. These molecules are comprised of an alkyl chain with a sulfur end group. Sulfur chemically bonds to gold and silver surfaces. Therefore when the alkanethiol comes in contact with either surface, the molecules self assemble to form a monolayer.

The two most widely used methods of depositing SAMs on a substrate are (1) immersion of the substrate into a reactant solution of the molecules and (2) vapor-phase deposition of the molecules onto the substrate. In each method, the exposure time and flux of the molecules are the key parameters that govern the coverage. The immersion technique

produces a monolayer by simply placing the substrate into the reactant solution for a controlled period of time. The vapor deposition technique consists of a substrate strategically positioned near the reactant solution. The substrate can be placed either upside-down (thus facing the source of the diffusing molecules) or along side of the source. In the work described in this thesis, the latter method will primarily be used to make an in-plane homogeneous SAM layer. Further, the vapor deposition approach can be modified to vary the molecular coverage across the surface of the substrate (Figure 1.3). In this technique, the substrate will be placed horizontally next to a diffusing source comprising the SAM precursors. As the molecules leave the diffusing source, they form a concentration gradient in the vapor phase, which subsequently “imprinted” onto the substrate thus forming a monolayer with position-dependent concentration of molecule in the SAM.

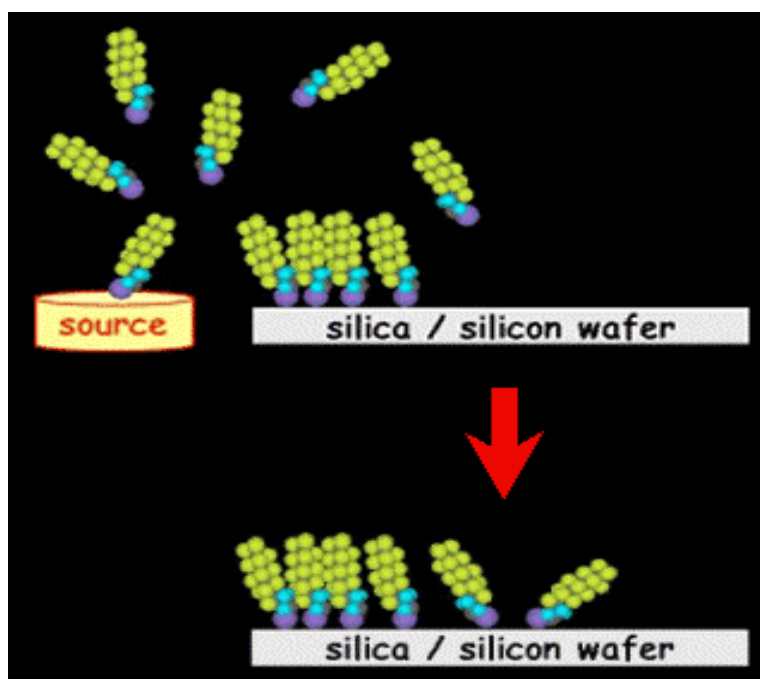


Figure 1.3: Illustrates the diffusion of source molecules to a silica/silicon wafer form a molecular gradient. Image courtesy of J. Genzer.

Molecular gradients are of interest because of the wide variety of applications which can be used such as selective adsorption,^{11,12} gradient templating,¹³⁻¹⁶ controlled motion of liquid droplets,^{9,17} particle sorting,¹⁸ and many others. Thus developing techniques that lead to the formation of molecular gradients have been extensively reported.^{11, 19-21} These include vapor deposition, soft lithography techniques and mechanical distribution techniques^{7,8} Choi and Newby developed a contact printing technique that produced a micrometer-scale gradient surface using an elastomeric stamp.⁶ Creation of a “double molecular gradient” has also been shown by Genzer et al.⁷ Double molecular gradients are formed using two sources of reactants, which diffuse across a single substrate.

The chemical composition of surface gradients can be characterized by numerous analytical techniques, including infrared spectroscopy, ellipsometry, scanning force microscopy and using a quartz crystal microbalance.^{3, 1} These techniques provide information about the position-dependent chemistry, molecular orientation, and coverage. With the use of a contact angle goniometer, contact angle measurements can also measure wettability as a function of position, which is indicative of surface composition. Contact angle measurements along the surface of a substrate can indicate areas of differing hydrophobicity / hydrophilicity indicated by higher / lower contact angles on a chemically modified surface. As a gradient progresses from hydrophobic to hydrophilic, the contact angle of water with the surface progresses from higher to lower.

1.1.2 Motion of Liquid on Gradients

Wettability gradients can facilitate the motion of liquids across a substrate as the result of the variability in the interfacial energy between the substrate and the liquid.⁸ If the droplet of liquid is large enough to experience a sufficient variability across it, an imbalance of surface tension forces on opposite sides of a droplet will promote its movement to the region of lower interfacial energy.¹ For droplet motion to occur, it is not only imperative to design a proper wettability gradient but also to have a low contact angle hysteresis. Droplet motion should occur when “the minimum receding contact angle at one edge of the drop is greater than the maximum advancing contact angle at the other edge”.⁸ A large hysteresis increases the difference between the advancing and receding edge of the drop, which, in turn, slows down or completely inhibits the movement of the droplet.

In 1992 Chaudhury and Whitesides were able to create an imbalance of surface tension forces on a droplet⁹ by producing a wettability gradient that propelled the water droplet up an inclined plane. The gradient was prepared using a silicon substrate and n-octyldecyl trichlorosilane (OTS) SAM with the vapor deposition technique. Bain and Ondarcuhu reported that rapid motion of liquids over longer distances was achievable if a wettability gradient was created dynamically by a chemical reaction at the liquid/solid interface.^{10,11}

In a gradient, the droplet cannot reverse its path along the chemical gradient. To overcome this limitation, electrical and photochemical approaches were designed to alter dynamically the chemical functionality presented at the surface and thus to create reversibility in the wettability along the surface. For example, Abbott and coworkers

developed an electrochemical method using a redox-active surfactant based on ferrocene. A reduction of ferrocenium to ferrocene lowered the hydrophilicity of the surface, thus generating a surface tension gradient. The surface tension gradient then could be used to pump liquids reversibly along a channel.¹² In a second example of a dynamically adjustable gradient, Ichimura and coworkers used a photoresponsive molecular gradient and ultraviolet (UV) light to develop a reversible method for droplet motion.¹³ Both the direction and velocity of the droplet in motion were controlled by varying the direction and steepness of the gradient in light intensity. A surfactant containing a light sensitive azobenzene moiety was physisorbed to a substrate. Exposure to UV light caused the azobenzene moiety to isomerize between its cis and trans forms. Azobenzene has one of two isomeric states (cis or trans) depending on the wavelength of light used to illuminate the surface. When UV radiation of 365nm was shined on the monolayer, the trans isomer absorbed this light and was transformed to the cis isomer. This process could be reversed. The cis isomer could be transformed to the trans isomer by applying a wavelength of 436 nm.

In another example, Daniels, et al reported an increase in the velocity of a drop on a surface due to a wettability gradient in the presence of condensation.¹³ More specifically, the coalescence of droplets in conjunction with the fast removal of heat from steam condensing on a gradient surface resulted in droplet speeds ranging from 20 to 40 $\mu\text{m/s}$. These demonstrations rely on both the presence of additional energy and gradient surface tension imbalance to create a driving force that enhances the velocity of the drop.

1.2: Surface Modifications: Surface Tethered Polymers

1.2.1: Polymer Thin Films

In the discussion above, small molecules of discrete size were used as the components of a thin film. An alternative for the modification of a surface is to alter its physico-chemical properties is the application of a thin polymer film. These tailored surfaces are used, for examples, for corrosion resistance, responsive materials, and photolithographic masks.²⁵ Polymer thin films can be physisorbed or chemisorbed to a material surface. Polymer films from solution can be obtained by using spin casting or dip-coating methods. Another approach is growth of the polymer film off of the surface using a surface-bound polymerization initiator that can react with monomer molecules exposed to it (See Figure 1.4) Both techniques are widely used and have different capabilities and attributes.

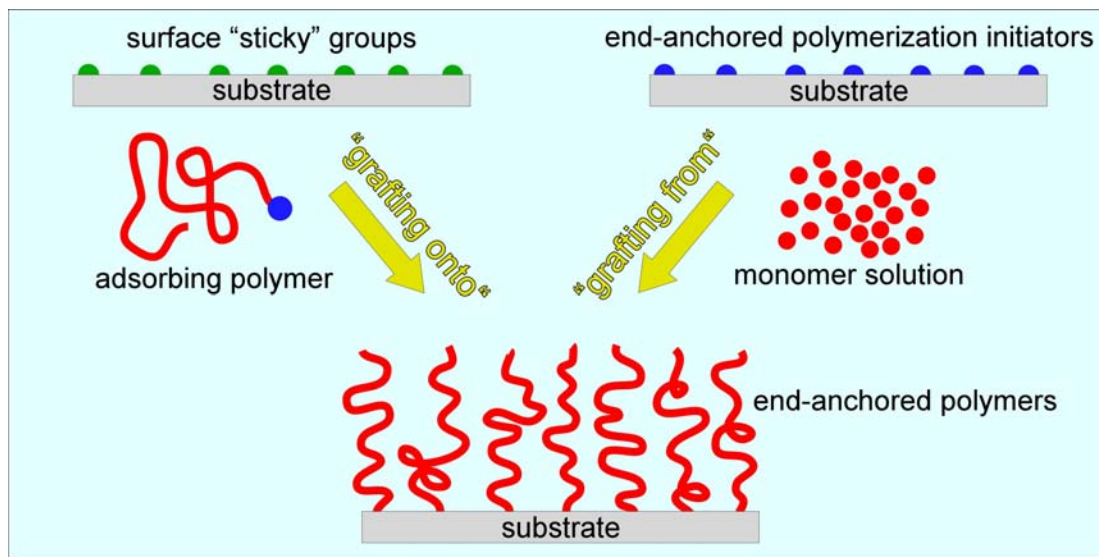


Figure 1.4: Illustration of two types of polymer film formation: grafting onto, and grafting from. (Illustration courtesy of J. Genzer)

1.2.2: Surface Based Polymerization

Surface tethered polymers consist of polymers with reactive end groups being grafted onto or from surfaces, resulting in a “polymer brush”. Polymer brushes formed by grafting “onto” a substrate are generally prepared via chemical bond formation between reactive groups on the surface and reactive end groups on the polymer chain. This technique has the advantage of a well-characterized chain length of the grafted polymer. However, due to steric hindrance of the reactive surface sites, this technique provides low grafting density of the polymer chains to the surface. Polymer brushes grafting “from” or surface- initiated polymerizations are used to overcome the low grafting density. In order to form high surface density tethered polymer chains, surface-bound polymerization initiators formed via self-assembled monolayers are exposed to a monomer solution, resulting in a high surface density of tethered polymer chains.

To achieve maximum control over brush density and composition, a controlled polymerization is highly desirable. Several controlled polymerization techniques have been used to grow polymer brushes including living ring opening polymerization, living cationic polymerization, reversible addition- fragmentation chain transfer polymerization and atom transfer radical polymerization.²⁶ Of these, controlled living radical polymerizations have become the most favored route due to less stringent experimental conditions as well as the compatibility with a wide range of functional monomers. Section 4.2.1 discusses atom transfer radical polymerization in detail.

The conformation of the surface tethered polymers can be very important in governing the behavior of the polymer coating in a given application and depends upon the environment around the polymer brush. Good solvent conditions (favorable interaction between the monomer and solvent molecules) form an expanded coil. The favorable interactions between the molecules supercede that of the loss of entropy due to chain stretching. Inversely, polymer brushes in poor solvents form a collapsed globule. There is an intermediate between good and poor solvent environments, which takes the shape of a mushroom conformation. However, in applications it is not always useful or possible to control polymer conformation with environmental variables. Thus, it is desirable to design a system that dictates the conformation by controlling the molecular weight and the grafting density of the polymer chains to the surface. To this end, Tomlinson et al designed a gradient substrate to vary the properties of the polymer surface continuously across the substrate between two extreme values.²⁷ They used a solution draining method of exposing the initiated surface to the monomer solution, thus forming a gradient of initiator density. The steepness of the gradient was determined by the reaction time of the polymerization. The system can be used to vary molecular weight and grafting density on a single sample. In Chapter 4, this system will be used to vary the polymer brush thickness in preparation for DNA attachment.

1.3: Surface Modifications: Charge Modification

1.3.1: Polled Lithium Niobate

Ferroelectric and other polar materials have been used in a number of applications including piezoelectric sensors, imaging devices and capacitors. Furthermore, ferroelectrics have

nonlinear optical properties, which are of increasing interest as the area of integrated optics continues to expand. Lithium niobate is already being recognized as a metal oxide of choice for several industries because high quality single crystals can be grown reproducibly. Single crystals of LiNbO_3 are uniaxial crystals, with a polarization vector that can align in two directions. The direction of this alignment can be controlled by application of an external electric field (a process known as poling). This results in a bulk dipole at the surface. However, experimental data exists that indicates that electrical polarization can be detected. Could this electrical dipole be used as a stimulus for self-assembly? Chapter 5 will discuss some preliminary experiments to determine if molecules will assemble on a polarized, patterned ferroelectric substrate. Self-assembled molecules will be used throughout each area of the following chapters with regards to liquid transport, tethered polymers and polar substrates.

1.4: References

1. DeGennes, P.; Brochard-Wyart, F.; Quere, D. *Capillarity and Wetting Phenomena*; Springer Press: NY, 2002.
2. Brochard, F. *Langmuir* **1989**, 5, 432.
3. Ulman, A. *An Introduction to Ultrathin Organic Films*; Academic Press: CA, 1991.
4. Dertinger, S.; Jiang, X.; Li, Z.; Murthy, V.; Whitesides, G. M. *Proc Natl Acad Sci* **2002**, 99, 12542-12547.
5. Chaudhury, M. K.; Whitesides, G. M. *Science* **1992**, 256, 1539.
6. Bain, C. D.; Burnett-Hall, R.; Montgomerie *Nature* **1994**, 372, 414.
7. Ruardy, T. G.; Schakenraad, J. M.; van der Mei, H. C.; Busschner, H. J. *Surf. Sci. Rep.* **1997**, 29, 3.
8. Clare, B. H.; Efimenko, K.; Fischer, D. A.; Genzer, J.; Abbott, N.L. *Chem. Mater.* **2006**, 18, 2357
9. Bhat, R. R.; Fischer, D.A.; Genzer, J. *Langmuir* **2002**, 18, 4142
10. Plummer, S. T.; Bohn, P. W. *Langmuir* **2002**, 18, 4142
11. Bhat, R. R.; Chaney, B. N.; Rowley, J.; Liebmann-Vinson, A.; Genzer, J. *Adv Mat.*, **2005**, 17, 2802
12. Bhat, R.R.; Tomlinson, M. R.; Genzer, J. *Macromol. Rapid Commun.* **2004**, 25,270
13. Daniel, S.; Chaudhury, M.K.; Chen, J.C. *Science* **2001**,291 633
14. Petrie, R.; Bailey, T.; Gorman, C.; Genzer, J. *Langmuir*, **2004**,20 9893-9896
15. Ionov, L.; Stamm, M.; Diez, S. *Nano Lett.* **2005**, 5, 1910

16. Genzer, J. Molecular gradients: Formation and applications in soft condensed matter science. In Encyclopedia of Materials Science; Buschow, K. H. J., Cahn, R.W., Flemings, M.C., Ilshner, B., Kramer, E. J., Mahajan, S., Eds.; Elsevier: Oxford, 2002
17. Genzer, J. ; Bhat, R.R.; Wu, T.; Efimenko, K. In Molecular gradient nanoassemblies; Nalwa, H. S., Ed.; American Scientific Publishers: Stevenson Ranch, CA, 2004.
18. Genzer, J. J. Adhe. **2005**, 81 ,417
19. Genzer, J.; Fischer, K.; Efimenko, K. *Applied Physics and Letters* **2003**, 82, 266.
20. Bain, C. *ChemPhysChem* **2001**, 2, 580.
21. Choi, S.; Newby, B. *Langmuir* **2003**, 19, 7427.
22. Ondarcuhu, T.; Domingues Dos Santos, F. *Phys.Rev.Lett.* **1995**, 75, 2972.
23. Shin, J. Y.; Abbott, N. L. *Langmuir* **1999**, 15.
24. Ichimura, K.; Oh, S. K.; Nakagwa, M. *Science* **2000**, 288, 1624.
25. Garbassi, F., Morra, N., Occhiello, E., Polymer Surfaces: From Physics to Technology, (J. Wiley & Sons, New York)
26. General Reference of polymerization techniques
27. Tomlinson, M., Bhat, R., Genzer, J. , Polymer Preprints **2005**, 26 (2), 44

Chapter 2: Liquid Transport: Modification of Surface Topography to Reduce Friction at the Liquid/Substrate Interface

This chapter has appeared in publication form

Petrie, R.; Bailey, T.; Gorman, C.; Genzer, J. *Langmuir*, **2004**,20 9893-9896

2.1 Project Goals and Motivation

In this chapter, the motion of water droplets on surfaces decorated with molecular gradients comprising semi fluorinated (SF) organosilanes is described. SF molecular gradients deposited on flat silica substrates facilitate faster motion of water droplets relative to the specimens covered with an analogous hydrocarbon gradient. Further increase in the drop speed is achieved by advancing it along porous substrates coated with the SF wettability gradients. The results of our experiments are in quantitative agreement with a simple scaling theory that describes the faster liquid motion in terms of reduced friction at the liquid/substrate interface.

2.2 Introduction

Practical studies of liquid movement across substrates have enhanced our understanding of several academic and industrial fields such as microfluidics, biosensors and drug delivery. Controlling wetting properties and topography of surfaces can facilitate faster and more efficient ways of moving liquids. Specifically, altering these parameters can affect the speed and mechanism by which the droplet travels on a substrate.¹⁻¹³ A liquid droplet placed on a surface bearing a spatial chemical heterogeneity can traverse in the direction of

the lower contact angle because of the imbalance of surface energies acting on various parts of the droplet and the tendency of the droplet to establish a new equilibrium. Chaudhury and Whitesides demonstrated this concept of controlled drop motion driven by variable wettability originating from the substrate. They showed that a liquid drop can move along a wettability gradient and in some circumstances can even climb up an inclined plane.¹ In their seminal paper, Chaudhury and Whitesides also recognized the importance of contact angle hysteresis, *i.e.*, the difference between the advancing and receding contact angles, on the drop motion. Specifically, they identified that liquid movement occurs when the receding contact angle of the back (receding) edge of the drop is larger than the advancing contact angle of the front (advancing) edge of the drop. However, contact angle hysteresis will serve to reduce the difference between the advancing and receding edge of the drop, therefore possibly slowing or halting drop motion. To overcome the latter problem, Daniel and Chaudhury used an external force by supplementing the chemical gradient driving force with an in-plane vibration of the drop.² They demonstrated that substrate vibration helped to overcome the relatively large contact angle hysteresis ($\approx 20^\circ$) thus increasing the drop velocity up to ≈ 5 times.

Recently, Daniel and coworkers provided more insight about the various molecular parameters that influence the motion of liquid drops on chemically heterogeneous surfaces.³ They argued that the drop velocity (v) is related to the surface tension of the liquid (γ), the radius of the droplet on the surface (R), and the position-dependent change of wettability:^{2,3,4}

$$v \cong \frac{\gamma R}{\eta_s} \frac{d \cos(\theta)}{dx} \quad (1)$$

In Equation (1) θ is the contact angle of the liquid with the substrate and η_s represents a viscosity parameter that denotes the friction at the liquid/solid interface.⁴ Defining the

capillary number as $Ca=v/v^*=v\eta/\gamma$, where v^* equals the surface tension (γ) divided by the liquid bulk viscosity (η), Equation (1) can be rewritten as:

$$Ca = K \cdot R \frac{d \cos(\theta)}{dx} = K \cdot R^* \quad , \quad (2)$$

where the coefficient K accounts for the corrections to η due to the frictional forces at the liquid/solid interface, and $R^* = R \frac{d \cos(\theta)}{dx}$. Daniel and coworkers demonstrated the general validity of Equation (2) by studying the motion of droplets of various liquids on surfaces covered with a molecular gradient made of self-assembled monolayer of $H_3C(CH_2)_{9SiCl_3}$ (H10-SAM) prepared on flat silica-covered substrates. Data of Ca vs. R^* from 4 different liquids had approximately identical slopes, indicating that K was very similar in all cases studied and was presumably dictated primarily by the surface energy of the substrate. They also established the effect of the contact angle hysteresis on the droplet motion. Daniel and coworkers showed that in the Ca vs. R^* plot the hysteresis appeared to cause only a change in the intercept in the data but not the slope. By utilizing this approach, the researchers were able to visually separate the effect of friction and contact angle hysteresis on drop motion. Specifically, the findings of Daniel and coworkers indicate that, regardless of the hysteresis, the velocity of the droplet will increase (hence the slope in the Ca vs. R^* plot increases) when the friction at the liquid/solid interface decreases.

From this perspective, one can reason that higher drop velocities can be achieved by lowering the frictional forces experienced by the drop as it traverses the gradient. This concept contrasts with the earlier focus² on overcoming hysteresis to maximize the velocity of the drop. Because of low surface energy and low friction of fluorine moieties, liquid droplets moving along surfaces comprising variable density of fluorinated groups should

move faster, relative to the motion of a droplet moving on an analogous hydrocarbon surface. Moreover, the friction may be further decreased at the liquid/solid interface by utilizing substrates with small pores that cannot be wet by a moving liquid. Quéré and Bico have shown that wettability at the liquid/solid interface can be lowered if air is trapped below the liquid in the holes of the rough surface. In such a situation, the liquid positions itself on the surface in a similar fashion as an Indian “fakir” lying on the points of a bed of sharp nails.^{16, 17, 18} The contact angle (θ^*) of a “fakir” droplet residing on such physically rough substrates is given by:¹⁶

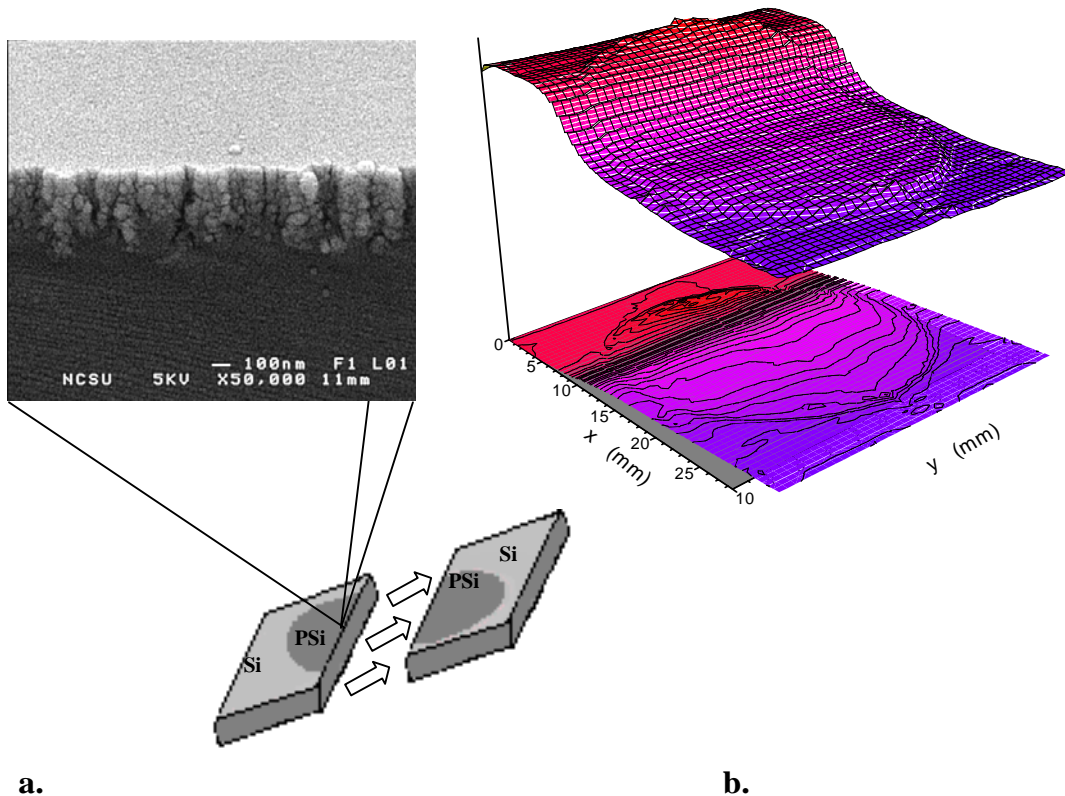
$$\cos(\theta^*) = -1 + \phi_s (\cos(\theta) + 1) \quad , \quad (3)$$

where ϕ_s is the fraction of the liquid/solid interface below the drop. Such a situation should facilitate a decrease in the friction and a corresponding increase in velocity of the droplet because of the decreased contact area at the liquid/solid interface.

In the work described in this chapter, we utilize the above two concepts in facilitating fast motion of water droplets across a surface-bound wettability gradient. First, we measure the velocity of water droplets on molecular gradients made of semifluorinated SAMs on flat silica substrates and show that these are higher than the velocities observed by Daniel and coworkers on H10-SAM substrates. Next we demonstrate that further increase in drop velocity can be achieved by advancing water droplets along substrates comprising wettability gradients of semifluorinated SAMs that reside on top of porous substrates. Using a simple scaling model we demonstrate that the significant increase in the drop velocity on the porous substrates, relative to the motion on flat silica, correlates with the substrate porosity and hence reduced contact area at the solid/liquid interface.

2.3 Results and Discussion

Wettability gradients of semifluorinated molecules of heptadecafluoro-1, 1,2,2-Tetrahydrodecyl trichlorosilane (F8H2) were prepared on flat and porous silica substrates using the procedure outlined in the experimental section. Porous silica substrates were prepared by an electrochemical etch (for details see the experimental section) and imaged using scanning electron microscopy. Figure 2.1a highlights the cross-sectional morphology of the porous silica substrate. The spatial variation of fluorine concentration in the porous silicon specimen was established using combinatorial near-edge X-ray absorption fine structure (NEXAFS) spectroscopy.¹⁹ The results of the combinatorial NEXAFS experiments confirm that the surface is decorated with F8H2 molecules whose grafting density varies gradually across the sample. Moreover, the NEXAFS data reveal that the relative density of fluorine is higher in the porous region indicated by the elevated circle in the specimen. In contrast, the unetched area surrounding the porous medium reveals a lower concentration of F8H2. This result reflects the greater surface area within the porous region and indicates that the surfaces of the pores are (at least partially) filled with the F8H2 molecules.



a. **b.**

Figure 2.1: (a) Cross sectional scanning electron microscopy image of porous silicon. The diagram depicts the outline of the porous region after etching. (b) Relative fluorine concentration on the porous substrate decorated with the gradient in F8H2 self-assembled monolayer as determined from the combinatorial near-edge x-ray absorption fine structure spectroscopy experiments.

Given the previous emphasis on contact angle hysteresis, a comparison of the wettability of both the flat and porous surface was established using contact angle measurements. In Figure 2.2 we plot the advancing (θ_a) and receding (θ_r) contact angles of deionized water on both the flat and porous gradient surface. These angles were determined with the aid of imaging software from dynamic water contact angles measured at various positions along the substrate during droplet motion. These values were utilized to quantify

contact angle hysteresis (CAH). In this work, CAH is defined as $(\cos \theta_a - \cos \theta_r)$. The experimental values for CAH averaged across the substrate are $0.44 (\pm 0.025)$ and $0.58 (\pm 0.023)$ for the flat and porous substrates, respectively. Thus, the CAH is slightly higher on the porous substrate than on the flat substrate. This fortuitous behavior allows us to determine whether friction or CAH is most important in governing drop velocity across the gradient.

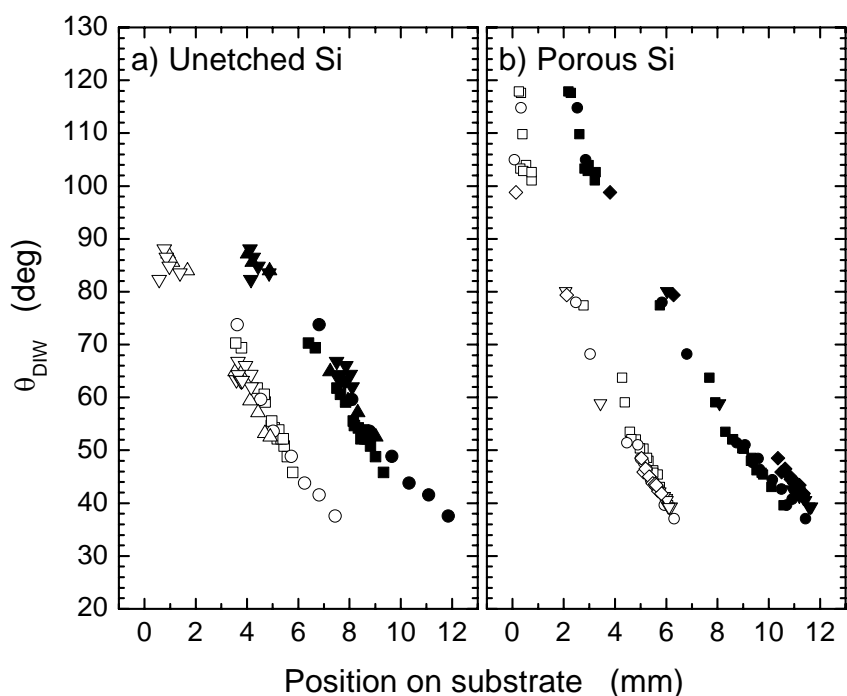


Figure 2.2: Advancing (solid symbols) and receding (open symbols) contact angles of deionized water as a function of the position on the F8H2 molecular gradient created on top of a flat (a) and porous (b) silicon substrate. The volume of the probing liquid was 4 (■), 6 (●), 8 (▲), 10 (▼), and 12 (◆) μ l.

Because v^* ($=\gamma/\eta$) is the same in all our experiments, the slope of the Ca ($=v/v^*$) vs. R^* plot provides a direct measure of the drop velocity. These slopes can be assessed from Figure 2.3, which shows the dependence of the capillary number on R^* for water droplets of various volumes (4 -12 μL) moving across flat (open symbols) and porous (solid symbols) substrates covered with the F8H2-SAM gradient. First, we compare the velocities of water droplets moving on flat substrates decorated with F8H2 gradients to those of the analogous hydrocarbon gradient.³ The slopes in the Ca vs. R^* plots are ≈ 0.015 and ≈ 0.007 for the F8H2 specimen and the hydrocarbon gradient, respectively, revealing the velocity of water drop is approximately twice as high as the F8H2 substrate relative to that on the H10 gradient. Next, we use the same analysis to determine how incorporating porosity into the substrate affects the drop velocity. The data in Figure 2.3 reveals that water droplets move faster along the F8H2 gradient created on the porous substrate relative to the F8H2 gradient on flat silica. The graph of Ca vs. R^* shows that the slope corresponding to the motion on the porous substrate is ≈ 0.035 . This is ≈ 2.3 times faster than the motion on the flat substrate covered with the same F8H2 molecular gradient.

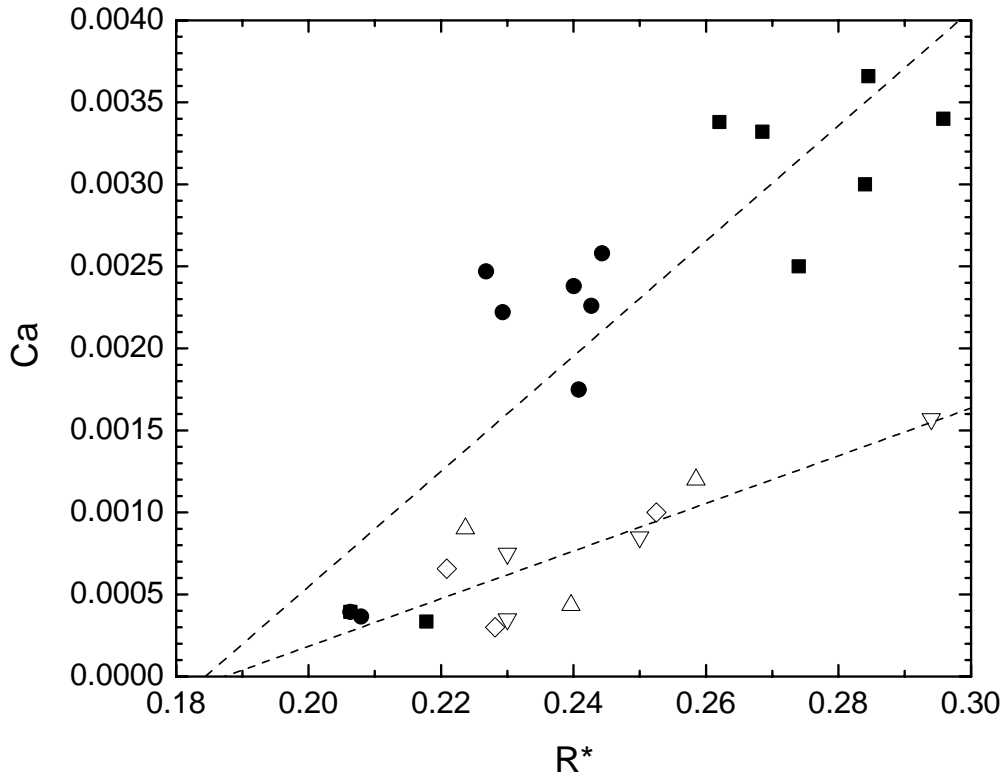


Figure 2.3: Capillary number ($Ca=v/v^*$) as a function of the normalized drop radius ($R^*=R \cdot \partial \cos(\theta) / \partial x$) associated with motion of a droplet of deionized water along the F8H2 molecular gradient created on top of a flat (open symbols) and porous (solid symbols) silicon substrate. During the course of the experiment the drop velocity was collected at multiple positions on the sample. The data presented in Figure 2.3 have been compiled from the drop velocity data collected at the constant contact angle of water equal to: 70° (∇), 65° (\triangle), 60° (\diamond), 100° (\blacksquare), and 80° (\bullet). The lines are meant to guide the eye.

If lower CAH were the primary force responsible for faster drop motion, one would expect that the CAH of the porous substrate were lower than that of the flat substrate. As discussed earlier, Daniel and coworkers infer the effect of CAH on the drop motion from the R^* intercept in the Ca . vs. R^* plot. From Figure 2.3, the close proximity of the R^* intercept

for the data collected on porous and flat substrates reveals that the CAH is approximately the same in both cases. This observation is in accord with our earlier conclusion, namely that the CAH on the porous substrate is similar to or slightly larger than that on the flat substrate (*cf.* Figure 2.3). Hence, the rapid increase of the drop velocity on the porous substrate relative to that on the flat surface must originate from a different effect, namely the reduced frictional forces at the liquid/substrate interface (*cf.* Equation 2).

2.4 Conclusions

Although there are some controversies regarding the friction of fluorinated surfaces,^{14,15} self-assembled monolayers made of fluorine-containing species are believed to provide surfaces with lower surface energy and lower friction. Our results seem to confirm the notion that the F8H2 surfaces possess lower friction and thus facilitate higher speeds of water droplets. Reduced friction at the liquid/substrate interface is also responsible for the observed faster motion of water droplets on porous substrates, relative to flat surfaces. Using the water contact angle on a homogeneous F8H2-SAM on the flat substrate ($\theta = 102^\circ$) and the corresponding contact angle of an F8H2-SAM on the rough substrate ($\theta^* = 125^\circ$), the fraction of the liquid/substrate interface below the drop (ϕ_s) is ≈ 0.5 (*cf.* Equation 3). Based on the work of Beake and Leggett, who established that the frictional forces on substrates made of mixed self-assembled monolayers scaled approximately linearly with the cosine of the contact angle,²⁰ we expect that the frictional forces between the drop and the textured substrate will reduce $\approx 1/\phi_s$ times.²¹ Hence, the slope in the Ca vs. R^* plot for motion on the rough substrate should be about twice of that on the flat substrate. From the data in Figure

2.3, the slopes are 0.035 and 0.015 for the rough and flat substrates, respectively, which gives a ratio of ≈ 2.3 , in reasonable agreement with the predicted value of ≈ 2 ($1/\phi_s$).

In spite of the simplicity of this scaling model (for convenience, we have neglected any additional contributions to the friction, such as the line tension at the air/liquid/solid interface), our analysis strongly suggests that the decreased contact area between the liquid and the porous substrate leads to the decreased frictional forces between the droplet and the substrate and results in the faster motion of droplets on the rough substrates relative to that on flat specimens. Combining chemical gradients with surface roughness offers a powerful method for controlling the movement of liquids on surfaces. For example, applications of rough surfaces for liquid movement may facilitate enhanced liquid removal capabilities. Advancements have been made in applying a thin non-wettable coating on windshields to remove rain droplets on vehicles, aircrafts, and virtually any glass surface. By tailoring the porosity of the glass this could in turn remove moisture droplets and contaminants at a faster pace and with greater efficiency. More in depth studies are underway to better understand the mechanism of motion for rough substrates.

2.5 Implementation / Experimental

2.5.1 Preparation of Porous Silicon

The porous silicon substrate was created by electrochemical etching a n-type silicon wafer (Sb-doped, 0.01-0.02 ohm·cm) in a Teflon cell, whose configuration was similar to the cell used by Siuzdak et al.²² The etching solution was a 1:1 (by volume) mixture of concentrated HF (49% Reagent Grade from Fisher) and absolute ethanol (100%, Fisher).

The cell compartment that contains the silicon and the etching solution is illuminated with $50\text{mW}/\text{cm}^2$ of white light from a fiber optic light source (Model I-150, Coherent, Inc.). While illuminated, about $4.6\text{ mA}/\text{cm}^2$ of constant current is passed through the cell chamber for one minute. After the etching process, the porous silicon sample is washed with absolute ethanol and dried under a nitrogen stream.

2.5.2 Preparation of F8H2 Gradient on Porous and Flat Surface

Our method closely follows that suggested by Chaudhury and Whitesides.¹ First, the substrate (porous or flat) was treated in an ultraviolet/ozone (UVO) chamber (Model 42, Jelight Company, Inc) for 20 minutes in order to generate a large number of the surface-bound hydroxyl groups necessary for the attachment of the semifluorinated organosilane molecules. A mixture of heptadecafluoro-1, 1,2,2-Tetrahydrodecyl trichlorosilane (95%, F8H2, Gelest, Inc.) and paraffin oil (1:3 w/w) was placed in a small container, which was positioned near the edge of the UVO-treated silicon substrate. During the gradient formation, the system was maintained in an enclosed chamber with controlled temperature ($22\text{-}24^\circ\text{C}$) and humidity (40-50%). As the F8H2 molecules evaporated, they diffused in the vapor and generated a concentration gradient, which was then imprinted onto the substrate. After 2-3 minutes, the sample was removed from the chamber, thoroughly washed with ethanol and dried with a stream of with nitrogen.

2.5.3 Characterization of the porous silicon surface

Combinatorial near-edge x-ray absorption fine structure (NEXAFS) spectroscopy measurements provided information about the spatial concentration of fluorine on the porous substrate.¹⁸ The experiments were performed at the National Synchrotron Light Source at Brookhaven National Laboratory. The samples were placed onto a four-degree of freedom goniometer, which allowed X-Y in-plane scanning of the sample in the soft x-ray beam. The partial electron yield (PEY) signal originating from the specimen was collected as a function the X and Y coordinates at the fixed angle between the sample surface and the electric vector of the x-ray beam ($=55^\circ$) at the three different energies of the x-rays: 680 eV (K pre-edge of fluorine), 692 eV ($1s \rightarrow \sigma^*_{C-F}$), and 720 eV (K post-edge of fluorine). The plot in Figure 1b was generated by standard normalization of the PEY data using the pre-, post-edge, and the $1s \rightarrow \sigma^*_{C-F}$ data.¹⁹

The morphology of the porous silicon specimens was probed using a scanning electron microscope (SEM, model Hitachi S-3200). Prior to the SEM experiment, the sample was sputter-coated with gold.

2.5.4 Measurement of contact angles and drop velocity

Drop movement was recorded using a CCD camera interfaced with a PC mounted perpendicular to a Rame-Hart 1000 goniometer stand. This CCD allowed for the recording of the drop motion in situ as the liquid was placed by a microsyringe on the gradient substrate. Measurements were then taken for the dynamic contact angle of the droplet on the substrate surface via Scion image software. The drawback of the aforementioned CCD

camera is that it was relatively slow speed and only had the ability to capture about 15 frames per second. The slow speed of the CCD camera resulted in the estimation of the position of the drop and thus created relatively wide scatter of the velocity data in the v/v^* vs. R^* plot.

Acknowledgments

The authors thank Dr. Dale Batchelor in the NCSU Analytical Instrumentation Facility for his contributions in field emission SEM. We also thank Dr. Kirill Efimenko (NCSU) and Dr. Daniel A. Fischer (NIST) for their assistance during the course of the NEXAFS experiments. NEXAFS experiments were carried out at the National Synchrotron Light Source, Brookhaven National Laboratory, which is supported by the U. S. Department of Energy, Division of Materials Sciences and Division of Chemical Sciences.

2.6 References

- 1) Chaudhury, M.K.; Whitesides, G.M. *Science* **1992**, 256, 1539.
- 2) Daniel, S.; Chaudhury, M.K. *Langmuir* **2002**, 18, 3404.
- 3) Daniel, S.; Sircar, S.; Gliem, J.; Chaudhury, M.K. *Langmuir* **2004**, 20, 4085.
- 4) Greenspan, H.P. *J. Fluid Mech.* **1978**, 84, 125.
- 5) Ondarcuhu, T.; Veyssie, M. *J. Phys. (Paris) II* **1988**, 1, 75.
- 6) Brochard, F. *Langmuir* **1989**, 5, 432.
- 7) Domingues Dos Santos, F.; Ondarcuhu, T. *Phys. Rev. Lett.* **1995**, 75, 2972.
- 8) Ichimura, K.; Oh, S.-K.; Nakagawa, M. *Science* **2000**, 288, 1624.
- 9) Daniel, S.; Chaudhury, M.K.; Chen, J.C. *Science* **2001**, 291, 633.
- 10) Lee, S.-W.; Laibinis, P.E.; *J. Am. Chem. Soc.* **2000**, 122, 5395.
- 11) Suda, H.; Yamada, S. *Langmuir* **2003**, 19, 529.
- 12) Choi, S.-H.; Zhang-Newby, B-m. *Langmuir* **2003**, 19, 7427.
- 13) Bain, C. *ChemPhysChem* **2001**, 2, 580.
- 14) Perry, S.S.; Lee, T.R. *Langmuir* **1999**, 15, 3179.
- 15) DePalma, V.; Tillman, N. *Langmuir* **1989**, 5, 868.
- 16) Bico, J.; Thiele, U.; Quéré, D. *Coll. Surf. A* **2002**, 206, 41.
- 17) Quéré, D.; Lafuma, A.; Bico, J. *Nanotechnology* **2003**, 14, 1109.
- 18) Quéré, D. *Nature Materials* **2002**, 1, 14.

19) Genzer J.; Fischer D. A.; Efimenko K. *App. Phys. Lett.* **2003** 82, 266

20) Beake, B.D.; Leggett, G.J. *Phys. Chem. Chem. Phys.* **1990**, 1, 3345.

21) Here we neglect any additional contributions to the friction arising from the line tension.

22) Shen, Z.; Thomas, J. J.; Averbuj, C.; Broo, K. M.; Engelhard, M.; Crowell, J. E.; Finn, M.G.; Siuzdak, G. *Anal. Chem.* **2001**, 73, 612.

Chapter 3: Liquid Transport: Effects of Surface Tension and Viscosity on a Viscous Droplet in Motion

3.1 Project Goals and Motivation

In today's society, there is growing interest in fundamental information on the physical parameters such as wetting and transport behavior of fluids that are made of two or more components. Physical properties such as surface tension and viscosity influence engineering and product design in many industrial applications such as food engineering, cosmetics, detergents, and coatings. Surface tension and viscosity are of importance because they affect the shape and hydrodynamic behavior of liquid droplets on surfaces. A low surface tension droplet on a substrate is indicative of strong molecular attractions at the liquid/solid interface and weak intermolecular forces within the liquid, which induce drop spreading. Viscosity describes a fluid's internal resistance as a result of interactions between liquid molecules. As stated previously, viscosity is a force that impedes droplet motion. Thus, the motion of a droplet on a hydrophobic surface is expected to increase as surface tension increases but decrease with increasing viscous force. Because liquid motion is important in a variety of processes, many research efforts have been centered on modifying the surface tension and viscosity of a solution with the intent of controlling this behavior.

Droplet motion of a high surface tension liquid with varying viscosities on a flat substrate was investigated. Chemical additives were used in order to maintain both a high surface tension and the ability to tailor the viscosity of droplets. Understanding how additives affect surface tension and viscosity and how these parameters affect the velocity of a moving droplet could lead to a way of controlling that velocity. These relationships can then be used

to control the motion of the droplet by adding an appropriate amount of an additive to the liquid.

Although chemical additives are commonly used to modify both the surface tension and viscosity of a solution, they also alter the composition of a homogeneous liquid. Introducing a chemical additive to a solution creates new molecular interactions within the combine solution, which can lead to changes in the molecular behavior at the liquid solid interface. This chapter will detail results on the effects of surface tension and viscosity of droplets in motion and provide insight on how homogeneity within a droplet affects its motion.

3.2 Introduction

3.2.1 Mechanisms to Induce Droplet Motion

The effect of both viscous and surface tension forces on the hydrodynamic droplet velocity has been predicted theoretically. Huethrost and Mara derived expressions for viscous and surface tension forces that oppose droplet movement down an inclined surface.² Their theoretical models provided a basis for experimental studies on drop motion on an incline. Subramanian et al. also provided a theoretical analysis of hydrodynamic resistance using the wedge approximation and lubrication theory.³ They concluded that the approximations for hydrodynamic force could be used to predict the quasi-steady state speed, independent of the driving force used to initiate the motion of the droplet.

The driving force of a droplet in motion can be generated mechanically or chemically. The substrate or liquid can be physically coaxed to induce droplet motion or chemical

modifications can be made on the substrate. In order to evaluate the effects of surface tension and viscosity on a droplet in motion, we address both mechanisms of induced motion. Within the scope of this paper, two general approaches to droplet motion will be pursued using a chemical gradient and tilted plane.

A common driving force for droplet motion involves creating a wettability gradient by chemically modifying a substrate. This phenomenon was first identified by Greenspan and Brochard^{4,5} and demonstrated experimentally by Chaudhury and Whitesides.⁶ Subsequently, several experiments have been reported using thermal, electrochemical, mechanical and photochemical methods to affect speed by which the droplet travels on a static wettability gradient.⁷⁻¹³ Recently, Yamada and Tada developed a method for reversible droplet motion by dynamically controlling the wetting gradient on a thin film electrode by applying an in-plane bias voltage to the substrate.¹⁴ This work illustrated an electrochemical driving force for liquids of varying viscosities.

Several methods of mechanically inducing droplet motion involve the use of an applied force. Daniel and co workers used vibration as a periodic force to drive the motion of a droplet across a substrate. They also provided insight about the various parameters such as viscosity, drop size and surface tension that influence the motion of liquid drops on heterogeneous surfaces.¹⁵ Their data revealed a linear correlation between the velocity and radius of the drop. They also noted that resistance of the moving contact line due to friction scales with the bulk viscosity of the droplet. Later, Petrie et al. demonstrated that the motion of a droplet could be increased by increasing the roughness of the substrate and thus reducing the frictional resistance at the liquid solid interface.¹

In this chapter, both a tilted plane and a chemical gradient will be used to induce the motion of droplets on a substrate so that the impact of both surface tension and viscosity on velocity can be correlated. By varying the concentration of sucrose in water, we have the ability to increase both the drop viscosity and the surface tension. Using droplet motion, it is documented here how the interplay between surface tension and viscosity influences the velocity of a multi-component viscous drop.

3.2.2 Contact Line Dynamics and Drop Composition of a Moving Droplet

Droplet motion can be coaxed as well as pinned by several factors affecting contact line dynamics.¹⁶⁻¹⁹ Natural processes such as raindrop motion on a hydrophobic glass windowpane exhibit droplet motion, which occurs by overcoming surface energy boundaries. Several types of droplet motion can often be seen simultaneously on the same window. These regimes include deformed drops of various shapes as well as drops that break up into lines of much smaller isolated drops. Observation of sliding droplets is a good indicator of a clean (e.g. defect free) windowpane surface. Contamination or marring on the windowpane results in a spatial variation in the equilibrium contact angle θ_e .

The Contact angle θ_e is formed within the liquid at the contact line, where the solid substrate, the liquid and the gaseous phase meet.¹⁶ A simple two-dimensional force balance is shown in (Figure 3.1). Figure 3.2 demonstrates that it is possible for the weight of the droplet to be balanced by the difference in the vertical component of the surface tension, if the upper contact angle is smaller than the lower one. It is possible therefore, for a drop to remain on the vertical plane, i.e. pinned to the surface.

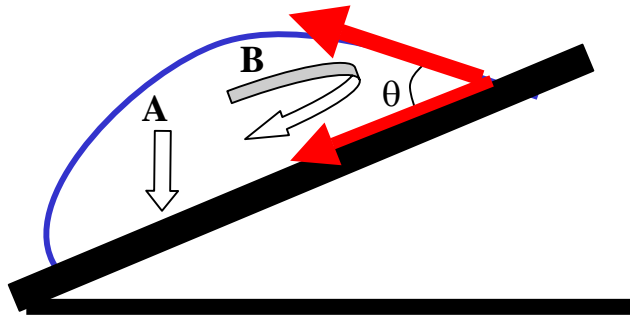


Figure 3.1: Diagram represents competing forces acting on a drop: weight or gravitational forces (A) and capillary forces (B). The weight of the drop is responsible for a downward pull of the droplet, while the capillary forces affect the internal flow within the droplet.

The shape and size of the droplet also dictate droplet motion. Capillary ($\pi r \gamma (\cos \theta_r - \cos \theta_a)$) and gravity forces (g) dictate the shape and area of contact with the solid of a stationary droplet on a horizontal substrate and inclined plane. In order for the droplet to retain a spherical shape, its radius must be smaller than the millimetric capillary length (k^{-1}).¹⁷ If not gravity will flatten the droplet. Second, smaller droplets often exhibit pinning on the solid due to contact angle hysteresis ($\Delta\theta = \theta_a - \theta_r$), with θ_a and θ_r the advancing and receding contact angles. Pinning occurs when the capillary force is larger than the gravitational force action on the drop ($\frac{4}{3}\pi R^3 \rho g \sin \alpha$), where R is the radius of the deposited drop and α is the tilting angle of the solid.

Marmur et.al concluded as the drop volume increases the “slip angle” or “roll-off angle” decreases.²⁰ Large drops with a radius greater than the capillary length ($R > k^{-1}$) tend to

maintain a constant velocity. However, due to the size and hysteretic effects of smaller droplets, large fluctuations in velocity are often observed.¹⁷

Controlling the degree of incline of the substrate with respect to the size of the droplet can be used to transition from a pinned droplet to a moving droplet. A low inclination angle can cause the droplet to remain pinned because of a dynamic critical phenomenon that occurs when the energy barrier due to a defect is not overcome.¹⁷ High angles of inclination cause the droplet to move beyond hysteric effects that cause pinning.

Our approach is to determine the optimal angle to incline a plane so that, when droplets rolled down it, gravitational forces overcome pinning. Systematic experiments were conducted to determine the optimal angle incline. In this chapter varying droplets are used down such an incline that the droplets reach a steady velocity determined by the balance between the rate of energy dissipation due to internal forces and the rate of change in gravitational potential energy.

3.3 Results and Discussion

3.3.1 Viscous Drop Motion on a Tilted Non-Wettable Solid and Chemical Gradient

Our goal was to study the motion of a liquid on a substrate in which the viscosity and surface tension of droplet could be varied systematically. Previously, we identified a need for fundamental studies on the effects of surface tension and viscosity on moving droplets. The quantitative results presented in our earlier paper¹ suggest that water droplets trap air pockets in porous silicon during their motion across a chemical gradient. Initially, we decided to further investigate this phenomenon by observing the behavior of a droplet with

varying viscosities as they travel across the chemical gradient on porous Si. Ethylene glycol was used because it is a homogeneous low surface tension liquid that is commercially available in varying viscosities. In a preliminary experiment conducted with droplets of ethylene glycol on a molecular gradient prepared on porous silicon, we noticed that these drops left material behind as they traveled across the gradient (Figure 3.2). It thus appeared that this liquid wetted the pores as it moved. This wetting is attributed to the lower surface tension of ethylene glycol compared to water. When water drops were studied the trail was not observed.

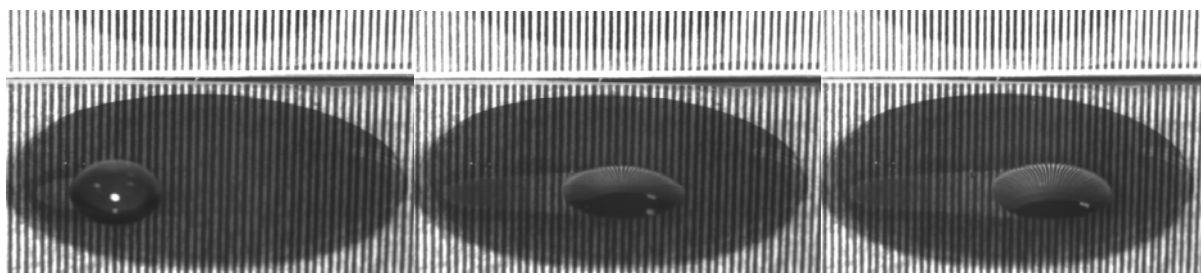


Figure 3.2: Image depicts a 30 μ L ethylene glycol droplet moving across a fluorinated gradient on Si. A trail is left behind as the droplet traverses the gradient substrate.

This wetting increased the interfacial area between the liquid and substrate, resulting in increased friction and reduced velocity. These results lead to the following question: How can this pore wetting be avoided? It is hypothesized that by increasing the viscosity of liquid droplet, the degree of pore wetting might be attenuated. Viscosity can affect both the velocity of the droplet across the substrate and wetting of the liquid into the pores in the surface. This then led to the question: If viscosity impedes droplet motion and an increase in surface tension reduces the friction of the droplet in motion how do these forces compete with each other? We realized these fundamental questions could be addressed by

determining the relationship between viscosity and surface tension in droplet motion and how they affect velocity.

Maintaining a high surface tension is important because it minimizes spreading on a surface. Aqueous sucrose solutions were used because of the ability to modify their viscosity while maintaining a high surface tension. The physical properties of sucrose/water solutions containing varying weight percentages of sucrose have been reported. Figure 3.3 shows the variation in the viscosity and surface tension of aqueous sucrose solutions as the concentration of sucrose increases. The viscosity of these solutions can be varied substantially, from 1.03 cS at 1 wt% sucrose to 45.5 cS at 60 wt% sucrose. Increasing the weight percentage of sucrose also increases the surface tension of the solution. However, this increase is comparably small (a change of 5.2 %).

A considerable number of computations have been reported on the physical properties of binary sugar-water solutions.²² Most of the studies deal with the dilute cases of only a few wt % of sugar in water. Investigations of concentrated mixtures are much fewer. Ekdawi-Sever et al. and Conrad et al have investigated sucrose aqueous solutions from 6-80wt% and higher.²³ Molinero et al were the first to identify a percolation threshold for the sucrose hydrogen-bonding network (HBN) between 33% and 40% w/w water.²⁴ They determined the resistance to shear deformation and mechanical stability of the mixture would increase upon formation of the sucrose network. This theory is significant to this work because the presence of the sucrose hydrogen-bonding network will alter the droplet in motion. We believe viscous forces will be a dominant force impeding droplet motion.

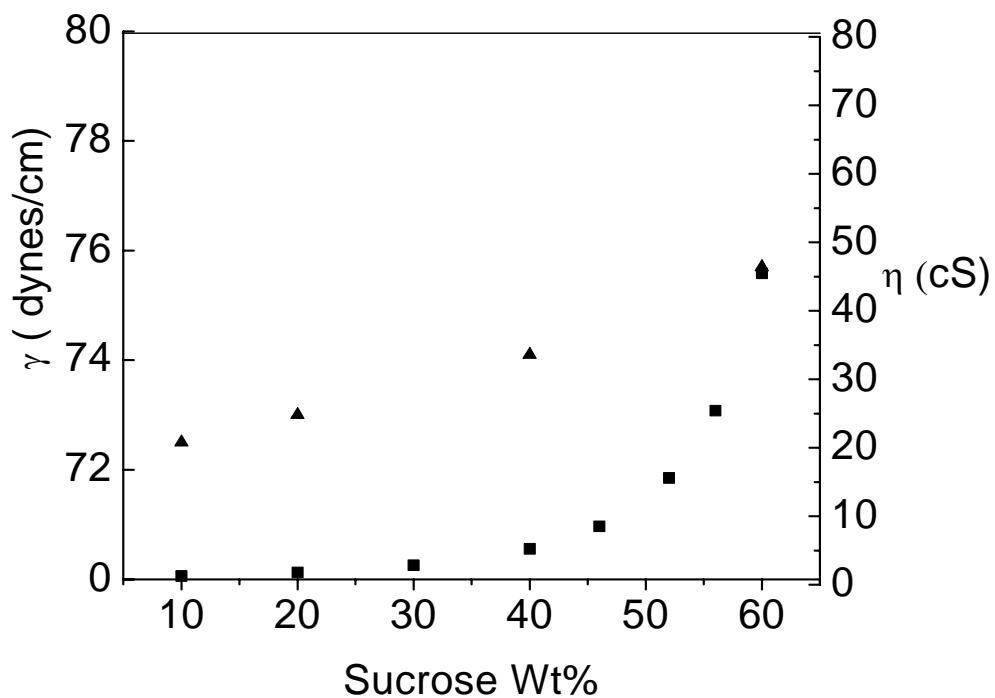


Figure 3.3: Graph depicting variation in surface tension (γ , ▲) and viscosity (η , ■) for aqueous solutions containing various weight percentages of sucrose at 25°C. Both an increase in surface tension and viscosity are shown as the sucrose concentration is increased. Values are taken from a published book of tables.²¹

To induce droplet motion, two types of substrates were used. In each case, these substrates were functionalized with semi fluorinated molecules of heptadecafluoro-1,1,2,2,-tetrahydrodecyl trichlorosilane (F8H2) that were vapor deposited on silica substrates to create a hydrophobic surface. From our previous work we have found self-assembled monolayers made of fluorine-containing species provide surfaces with low friction.¹⁵ A hydrophobic surface is needed to sustain a spherical cap drop conformation during droplet motion. In one set of experiments, these molecules were self-assembled to form a single

component homogenous monolayer. In a second set of experiments, a gradient in which the number of molecules varied in a given area was formed.

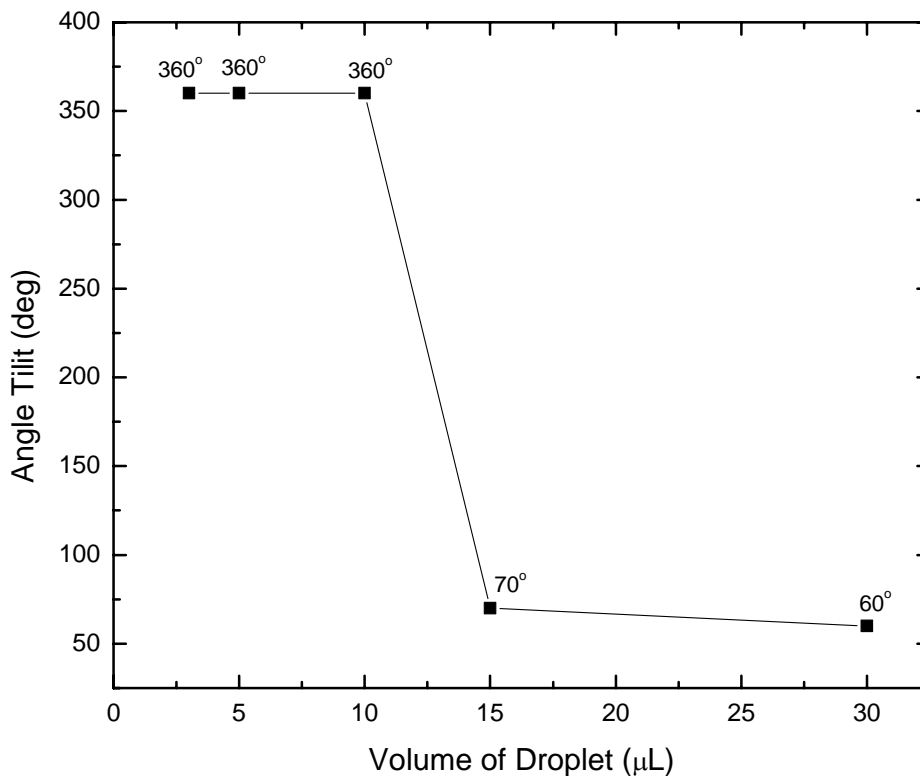


Figure 3.4: A graph depicting the relationship between the volume of H₂O droplets (3, 5, 10, 15, and 30 μL) and the tilt angle of a fluorinated homogeneous monolayer on Si substrate required to move them. The graph shows the tilt angle required to induce motion was achieved at 15 μL and 30 μL .

Before droplet motion experiments were conducted on the inclined homogeneous surface, initial experiments were done to determine the optimal volume and inclination angle for the chemically modified surface. This was done by placing a droplet of varying sizes on a

homogeneous F8H2 homogeneous monolayer and tilting the substrate until the droplet rolled off of the substrate. Results from Figure 3.4 indicate for the particular conditions used, the threshold volume required for droplet motion was not reached below 15uL. Droplets with volumes of 15 and 20uL showed movement at 70 and 60° angle tilts. This data shows the physical parameters for the droplet motion on incline experiments. The tilt angle indicates the “slip” angle at which the droplet began to move. A value of 360° indicates the drop on the substrate could be completely rotated without motion.

A 60° inclined plane was used to create a gravitational potential and provide an impetus for droplet motion of 30μL droplets across the homogenous self-assembled monolayer. The motion of droplets was analyzed using images obtained from a CCD Camera. Figure 3.5 illustrates the advancing and receding positions of droplets as they moved down a 60-degree inclined plane. From these data, the effects of surface tension and viscosity on velocity as the drop can be ascertained. The droplets used for analysis included water and aqueous sucrose solutions containing 10, 20, and 60-wt% sucrose (respectively, 1.00, 1.29, 1.80, and 45.5 cS). Little variation in the difference between the advancing and receding edge positions as the drop moved indicates little spreading of the droplet as it traverses the substrate. However the droplets clearly have different velocities.

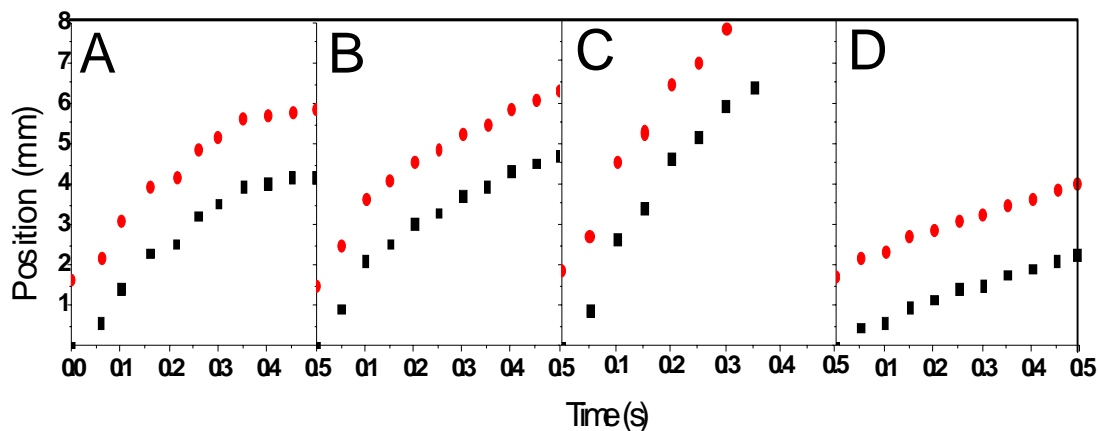


Figure 3.5: The advancing (●) and receding (■) positions of droplets containing varying sucrose concentrations plotted as a function of time. The sucrose concentrations are (A) 0 %, (B) 10 wt %, (C) 20 wt % and (D) 60 wt %, respectively

Figure 3.6 plots the velocity of 0, 10, 20, and 60 wt % aqueous sucrose droplets using the data from Figure 3.5. The velocity of the droplet containing 60 wt % sucrose is notably lower than the other sucrose solutions presented. Both droplets containing 10 and 20 wt % sucrose travel faster than the droplet containing no sucrose even though their viscosity is higher. This observation indicates that the increase in surface tension as sucrose is added to the water must be relevant to this behavior. As can be seen in Figure 3.6, the droplets composed of 10 and 20 wt % sucrose solutions show increases in velocity compared to the water droplet. Viscous forces overwhelm the effects of surface tension resulting in a decrease in velocity exemplified by a droplet of 60 wt % sucrose solution.

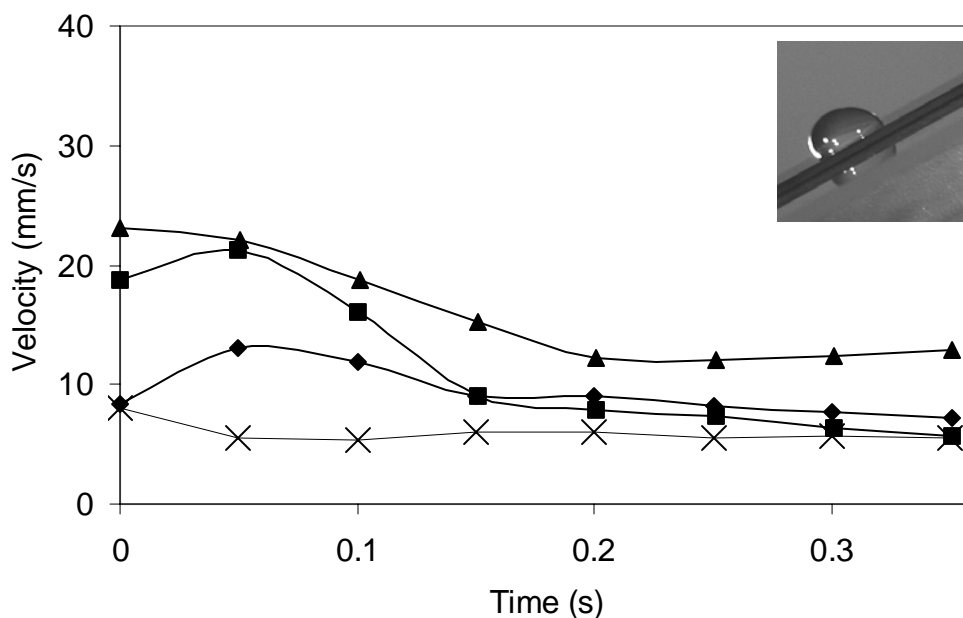


Figure 3.6: Graph of droplet velocity vs. time for droplets in motion on a 60° tilted substrate. The insert shows a photograph of a 20 wt % sucrose droplet in motion. Droplets contained (\blacklozenge) 0 wt %, (\blacksquare) 10 wt %, (\blacktriangle) 20 wt % and (\times) 60 wt % sucrose in water. Lines are drawn through the symbols merely as a guide to the eye. Velocity is measured immediately at the onsite of motion during liquid/ substrate interaction.

A second set of experiments employed an alternate method for inducing the droplet to move. A wettability gradient was prepared by time dependent vapor deposition of F8H2 molecules across a silica substrate (for details see Experimental Section). Contact angle measurements of water droplets held at fixed points along the substrate were taken and indicated the presence of a wettability gradient. The results of droplet motion on a gradient (Figure 3.7) reflect a similar trend in velocity with increasing sucrose concentration. Specifically, droplets containing up to 22 wt % sucrose moved faster than those containing less sucrose. The tradeoff in drop speed at 36 wt % coincides with the reported data range of

the higher activation energy for viscous flow caused by the sucrose hydrogen bonding network.²² As the sucrose concentration was raised further to 42 wt %, the velocity of the droplet continued to decrease.

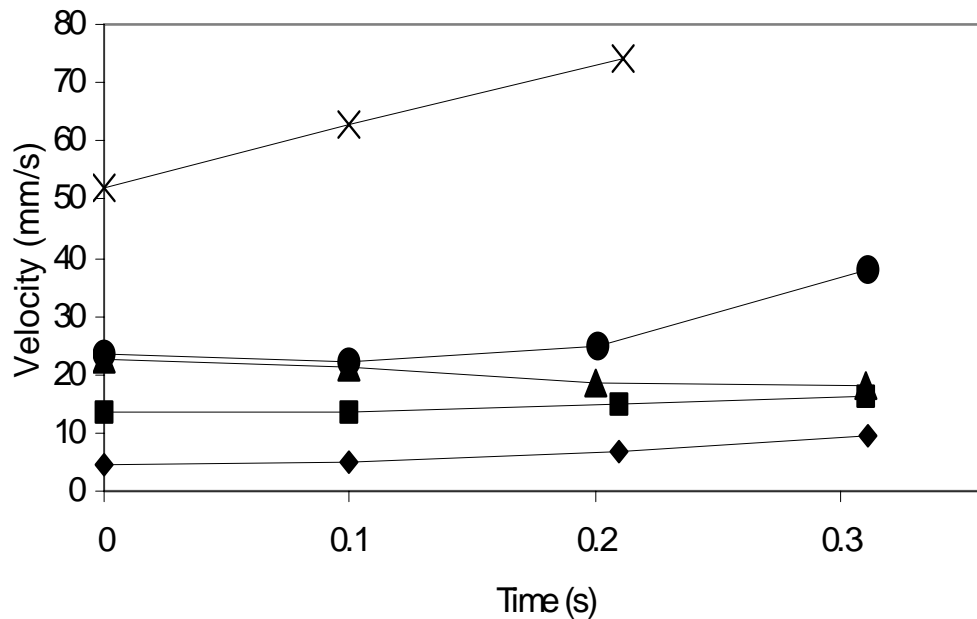


Figure 3.7: Graph of droplet velocity vs. time graph for droplets in motion on an F8H2 gradient. Droplets contained (♦) 0 wt %, (■) 10 wt %, (×) 22 wt %, (●) 36 wt % and (▲) 42 wt % sucrose in water. Faster motion for the 22 wt % solution resulted in collection of fewer points. Lines are drawn through the symbols merely as a guide to the eye.

Figure 3.8 shows the velocity measured for different aqueous sucrose droplets moving on a 60° tilted plane. Two regimes can be observed. For droplets containing lower than 42 wt % sucrose (0 - 6.1 cS) a higher velocity range can be observed. As the sucrose concentration is increased past 42 wt %, the range of velocity values decrease as well. These data again illustrate a change in droplet velocity. This observation suggests an increase in viscous force dominance after 42 wt % sucrose.

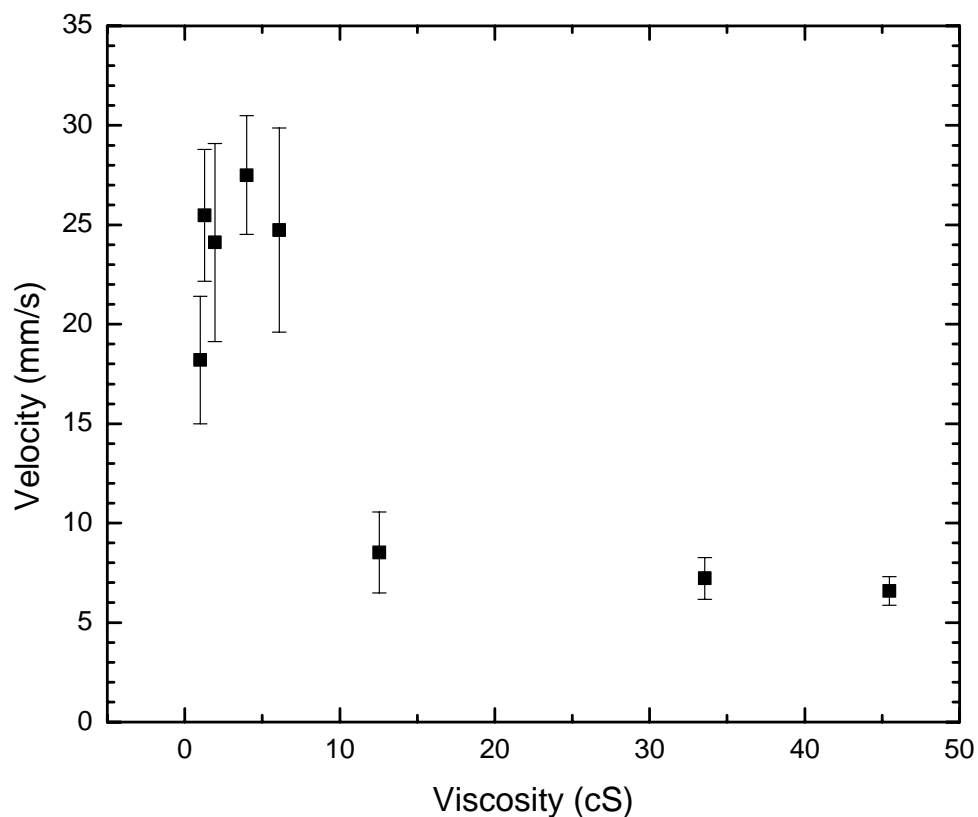


Figure 3.8: Graph of velocity vs. viscosity on a 60° tilted substrate. 30 μ L droplets of 0, 10, 22, 36, 42, 50, 58 and 60 wt % of sucrose were used.

Intuitively because of Newton’s law of viscosity, for a Newtonian fluid one would expect a linear decrease in the velocity as the viscous forces increase. Our results indicate a deviation from that expected, leading to the possibility of additional factors contributing to the observed, separate velocity regimes. Therefore we extended our studies to include an analysis on sucrose droplets of varying viscosities, along with substrates at varying tilt angles to determine trends in the data using a multi component liquid.

Kim et al were the first to suggest that steady sliding velocity of a “partially wetting” viscous drop on a specified surface can be determined by the linear relationship between capillary number and bond number in a low velocity regime.²⁴ Liamat et.al determined the $Ca (U\eta/\gamma)$ vs Bo_α relationship can be used to express the theory that the sliding velocity U increases with increasing substrate inclination angle (α).²⁵ This non-dimensionalized plot is used because the capillary number is based on the drop velocity U and the bond number used in the expression is the bond number tangential to the inclined surface, $Bo_\alpha = Bo \sin\alpha$ (where $Bo = \rho gr^2/\sigma$).

From our experimental results for a 30 μ l droplet on 20, 40 and 60° inclined planes the Ca vs. Bo_α values of these droplets were calculated and are shown in Figure 3.9. Figure 3.9 shows 0, 10, 20, 40 and 60 wt % sucrose droplets mostly increase in Ca as the Bo_α increases. It is also important to note the steep increase in Ca for 60 wt % sucrose. Although, 60 wt % sucrose droplets move slower than 0, 10, 20, and 40 wt % sucrose, the dynamic viscosity value is much larger for 60 wt % sucrose contributing to the increase in Ca . The dynamic viscosity value for 60 wt % is also higher than the sliding velocity used to calculate the capillary number.

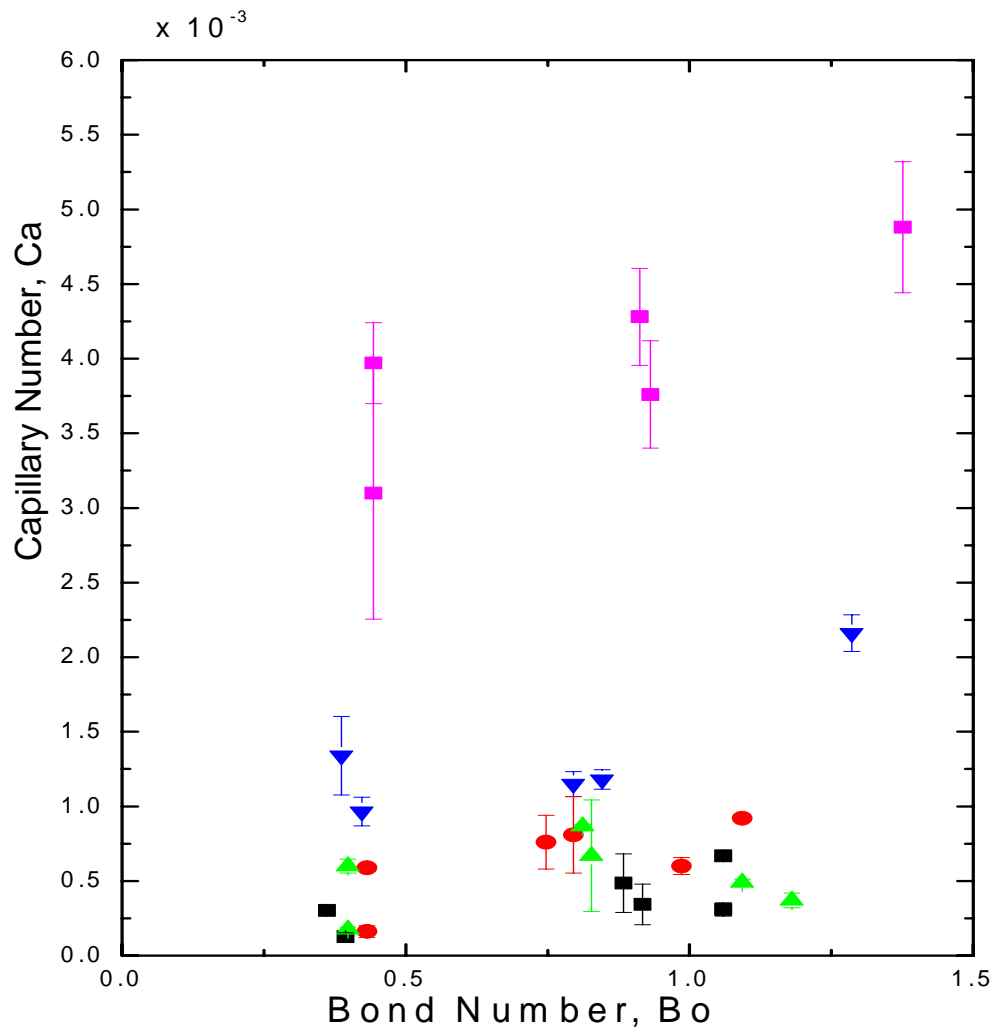


Figure 3.9: Depicts Ca vs Bo of 30 μL droplets moving on varying inclination angles (20, 40 and 60°). The data is represented as followed: 0 wt % (■), 10 wt % (●) 20 wt % (▲), 40 wt % (▼), and 60 wt % (◆).

3.4 Conclusions

This work presents a study on drop motion of a multicomponent liquid with competing interfacial effects. The following trends were shown in this work:

- (1) A decrease in the velocity of a moving drop (on an incline and gradient) was observed at 36 wt % sucrose concentration.
- (2) A high range of velocity was observed until viscous force dominance. This observation could be due to the increase in surface tension with increasing percentage of sucrose. This theory is difficult to address because the molecular behavior of the droplet on the surface is different from that of the bulk solution. Sucrose molecules in general are repelled by the water/ air interface, which leaves a thin periphery of water/ air molecules that surrounds the bulk fluid. This concept explains why polysaccharides, such as sucrose and glucose, can raise the apparent surface tension of water by a modest but non-negligible amount, when dissolved at fairly elevated concentrations. How this behavior affects a droplet in motion has not been reported.

An additional effect influencing the increase in drop motion can be attributed to friction. It is also known, that the higher the concentration of sucrose the thinner the zone depleted of sugar molecules. Therefore for lower concentrations of sucrose, the water / air interfacial area is larger. The water air interfacial area would be beneficial to this study because it has been reported that the addition of water molecules produces a decrease in friction²², which thereby could produce faster droplet motion.

3.5 Implementation/ Experimental

3.5.1 Surface Preparation

Silicon wafers (Sb-doped, 0.01- 0.02ohm-cm) were obtained from Silicon Valley Microelectronics. Strips of 35-40mm with no visible scratches were cut and cleaned from a silicon wafer. The strip was rinsed thoroughly with acetone, methanol, and deionized water (DI) and then placed in a sonic bath containing DI water for 10 minutes to ensure the removal of any debris and particles on the strip surface. The strip was then placed under ultraviolet ozone (Ultraviolet Ozone Chamber Model 42, Jelight Company, Inc) for 10 minutes to create hydroxyl groups on the Si surface. Finally the surface was dried with a jet of nitrogen and immediately used in preparation for self assembled monolayer formation. A 3:1 mixture of mineral oil and (heptadecafluoro-1, 1,2,2, Tetrahydrodecyl) trichlorosilane (F8H2) from Gelest was prepared. Silane vapor deposition was used to distribute diffusion molecules to the hydroxylated silicon surface. In preparation for the full coverage monolayer the silicon sample was fully exposed to the silane for a diffusion time of 3 minutes. For the gradient, only one region of the hydroxylated silicon wafer was exposed to the silane for 1.5 minutes. On the gradient substrate, locations on the surface that were closer to the silane source became relatively more hydrophobic (less wettable).

3.5.2 Measurement of Contact Angles

To ensure the formation of a self assembled monolayer, static contact angle measurements were taken before and after vapor diffusion of the silane. A Ramehart optical goniometer was used to conduct the measurements. A study was also conducted to

empirically determine the behavior of the fluorinated substrate once it was exposed to a polysaccharide liquid and removed. In this experiment contact angle measurements were taken before and after immersion in the liquid for 45 minutes. The substrates were then thoroughly rinsed with water and another set of contact angle measurements were taken. The contact angle measurements (degrees) were then recorded and averaged in Table 3.5.1. The data suggests within error (± 5 degrees) there is no appreciable change in the fluorinated surface structure upon interaction with the liquids.

Table 3.5.1: Contact angle measurements ($^{\circ}$) of deionized water, sucrose and glucose.

Liquid	Initial	After Immersion in Liquid	After rinsing with deionized water
Deionized water	112.4	110.97	111.7
40wt% Sucrose	112.6	112.13	107.87
40wt% Glucose	110.57	108.83	110.27

3.5.3 Measurement of Drop Velocities and Sizes

Drops of DI water, sucrose of varying concentrations, and a range of nominal volumes from 15-30uL were each introduced on a separate unused migration path on the strip at the beginning of the substrate. Their motion was captured using an image acquisition system. The video frames were acquired at a rate of 33 frames/s. The positions of both the advancing and receding ends of the migrating drop were tracked from one frame to the next using Scion Imaging software. The instantaneous velocity at a given position was calculated as the local slope of a straight line fitted to a set of points chosen symmetrically to the center of the drop's footprint on the position versus time curve.

3.5.4 Equipment

The angle tilt apparatus was specifically designed (T.Bailey) and constructed by (NCSU facilities) for the purpose of these experiments.

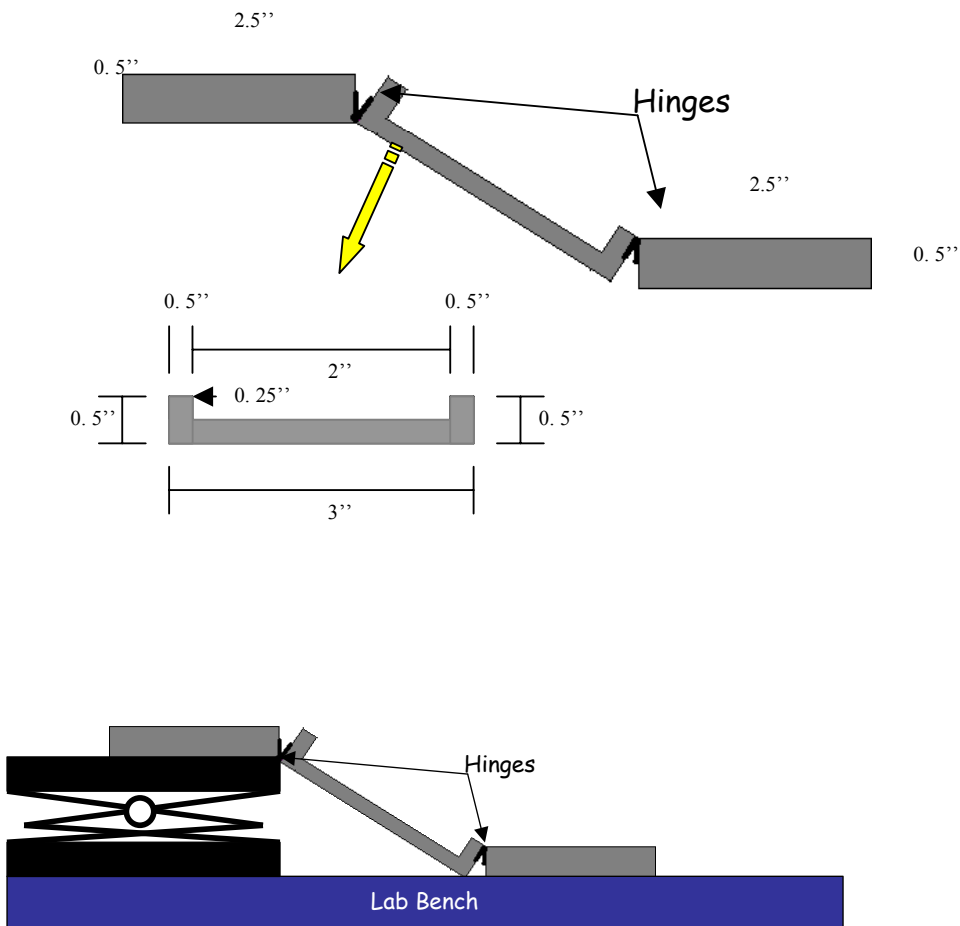


Figure 3.10: Depicts an angle tilt apparatus. The figures include dimensions and set up.

3.6 References

- (1) Petrie, R.; Bailey, T.; Gorman, C.; Genzer, J. *Langmuir* **2004**, *20*, 9893-9896.
- (2) Huethrost, J. M. *Langmuir* **1991**, *7*, 2756-2763.
- (3) Subramanian, R. M., N.; McLaughlin, J. *Langmuir* **2005**, *21*, 11844-11849.
- (4) Greenspan, H. P. *J. Fluid Mech.* **1978**, *84*, 125.
- (5) Brochard, F. *Langmuir* **1989**, *5*, 432-438.
- (6) Chaudhury, M. K. W., G. M. *Science* **1992**, *256*, 1539.
- (7) Ichimura, K.; Oh, S. K.; Nakagwa, M. *Science* **2000**, *288*, 1624.
- (8) Daniel, S. *Science* **2001**, *291*, 633.
- (9) Suda, H.; Yamada, S. *Langmuir* **2003**, *19*, 529.
- (10) Choi, S.; Newby, B. *Langmuir* **2003**, *19*, 7427.
- (11) Bain, C. *ChemPhysChem* **2001**, *2*, 580.
- (12) Cazabat, A. H.; Troian, S.; Carles, P. *Nature* **1990**, *346*, 824.
- (13) Gallardo, B. S.; Eagerton, F.; Jong, L.; Craig, V.; Abbott, N. *Science* **1999**, *283*, 57.
- (14) Yamada, S. *Langmuir* **2005**, *21*, 4254-4256.
- (15) Daniel, S.; Sircar, S.; Gliem, J.; Chaudhury, M. K. *Langmuir* **2004**, *20*, 4085.
- (16) Schwartz, L.; Roux, D.; Cooper-White, J. J. *Physica D* **2005**, *209*, 236-244.
- (17) Quere, D.; Richard, D. *Europhysics Letters* **1999**, *48*, 286-291.
- (18) Mahadevan, L.; Pomeau, Y. *Physics of Fluids* **1999**, *11*, 24492453.
- (19) Hodges, S.; Jensen, O.; Rallison, J. *J. Fluid Mech.* **2004**, *512*, 95-131.

- (20) Marmur, A.; Krasovitski, B. *Langmuir* **2005**, *21*, 3881-3885.
- (21) CRC Handbook of Chemistry and Physics (85th edition)
Taylor and Francis, Boca Raton, FL.
- (22) Lerbret, A.; Bordart, P.; Affouard, M.; Dascamps, M.; Migliardo *J. Phys. Chem B* **2005**, *109*, 11046-11057.
- (23) Ekdawi-Sever, N.; Conrad, P.B.; de Pablo, J. J. *J. Phys. Chem. A* **1999**, *103*, 4049
- (24) Molinero, V.; Cagin, T.; Goddard, W. *Chemical Physics Letters* **2003**, *377*, 469-474.
- (25) Kim, H.; Lee, H.; Kang, B. *Journal of Colloid and Interface Science* **2002**, *247*, 372-380.
- (26) Limat, L.; Grand, N.; Daerr, A. *J. Fluid Mechanics* **2005**, *541*, 293-315.
- (27) Oss, C.; Giese, R.; Docolis, A. *Colloids and Surfaces B: Biointerfaces* **200**, *19*, 147-162.

Chapter 4: Tailored Surfaces: Polymer Brush Gradients Synthesized via ATRP as a Platform for DNA Immobilization

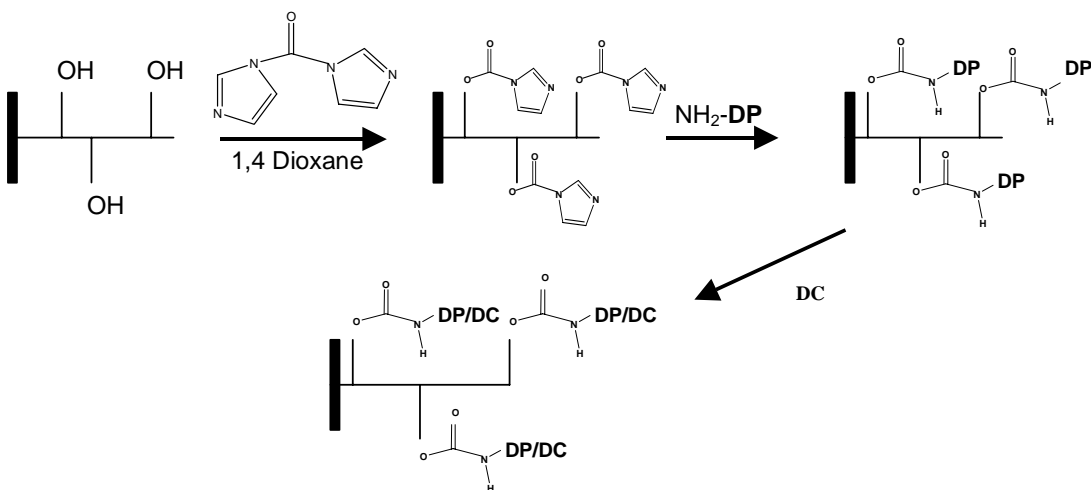
4.1 Project Goals and Motivation

DNA microarray technology is an emerging field that has captured the keen interest of chemists and biologists alike. Specifically, the development of biomolecular platforms for oligonucleotide immobilization and detection has attracted great interest. Recently, microarray substrates have been used for printing and storing nucleic acids and antibodies.¹ A DNA microarray is also known as a genome chip and is a collection of microscopic DNA spots attached to a solid surface, forming an array for the purpose of monitoring expression levels for thousands of genes simultaneously. Traditional genetic analysis methods were limited to single gene expressions in each experiment, but this technology provides a mean to analyze multiple genomes on a single chip.

Modifications have been made to the surface on which the microarray is constructed to enhance the efficiency in binding and detection of probe molecules.¹ The introduction of self-assembled monolayers has been advantageous to DNA immobilization because it created a uniform monolayer that increased the packing density of functional groups capable of binding to the DNA probe molecules along the surface.¹ However, despite this, there is still interest in further increasing the density of DNA probe strands in a given region of the surface. Detection of low concentrations of DNA might be improved with a greater density of probe strands. In order to increase the number of functional sites per unit area, dendrimers and polymers have been incorporated into the design of the microarray. Polymerization

techniques such as nitroxide-mediated and reversible addition fragmentation chain transfer polymerization have been previously reported.^{2,3} Here, surface initiated atom transfer radical polymerization will be utilized to synthesize a polymer brush suitable for DNA immobilization. The use of a polymer brush gradient to provide a systematic investigation on the optimal chain length of a polymer brush at a given grafting density. A polymer brush gradient on a substrate minimizes the polymeric materials and biological samples needed for analysis.

Scheme 4.1 provides an overview of the synthetic route used to achieve the proposed goals. The first step uses a coupling agent to functionalize the polymer brush, suitable for DNA binding. The amine terminated DNA probe is then reacted with the modified polymer brush. The final step involves the hybridization of a fluorescently labeled DNA target to the DNA probe on the polymer brush.



Scheme 4.1: Schematic illustration of oligonucleotide attachment via carbonyldiimidazole coupling to surface anchored polymer. DP represents DNA capture probe. DC represents the complimentary strand to DP with a fluorophore attachment.

4.2 Introduction

Nucleic acid analysis is a growing field because of the quest to map genomic sequences faster, using less complicated techniques in more cost efficient ways.³⁻⁶ Swami, *et al* demonstrated the ability to anchor thiol-terminated DNA SAMs directly to a gold surface.⁷ In addition they developed a two-potential electrochemical method to characterize the capture DNA probe and the hybridization probe. On silicon oxide based surfaces, Vandenberg *et al* used amino-propyltriethoxysilane (APTES) to create a single layer of functional sites suitable for oligonucleotide hybridization.⁸ This method was advantageous because of the mild conditions (solvents, room temperature, and reaction time) needed for SAM preparation.

Although SAMs offer a controlled method of functionalizing the substrate surface, SAM forming molecules are limited to accessibility only on the surface area of the substrate. To increase oligonucleotide density per unit area dendrimers were used as a platform of functional sites. Benters *et al* used PAMAM dendrimers to link oligonucleotides to an isothiocyanate functionalized glass surface.⁹ This immobilization technique displayed higher uniformity and reproducibility in comparison to detection on amino-silane coated glass.

This chapter investigates the use of surface anchored polymers as a method of increasing the density of immobilized biological molecules per surface unit area. Surface tethered polymers otherwise known as “polymer brushes” are tailorable, with varying mechanical properties and are amenable to functionalization along the polymer backbone.¹⁰⁻¹⁴ Polymer

brushes have also been used to alter surface properties such as biocompatibility,^{15,16} wettability,¹⁷ and friction.¹⁸

Recently, different types of polymerization techniques have been utilized to prepare polymer brush backbones for particle assembly. Wooley *et al* utilized controlled nitroxide mediated radical polymerization (NMRP) to form a polymer brush for streptavidin attachment.¹⁹ The final assembly was used for attaching biotinylated shell crosslinked (SCK) nanoparticles. Pirri *et al* utilized block copolymer brushes to immobilize oligonucleotides via radical addition-fragmentation transfer polymerization (RAFT).³ They observed that the use of a block copolymer assembly increased DNA hybridization efficiency compared to SAMs on glass substrates.

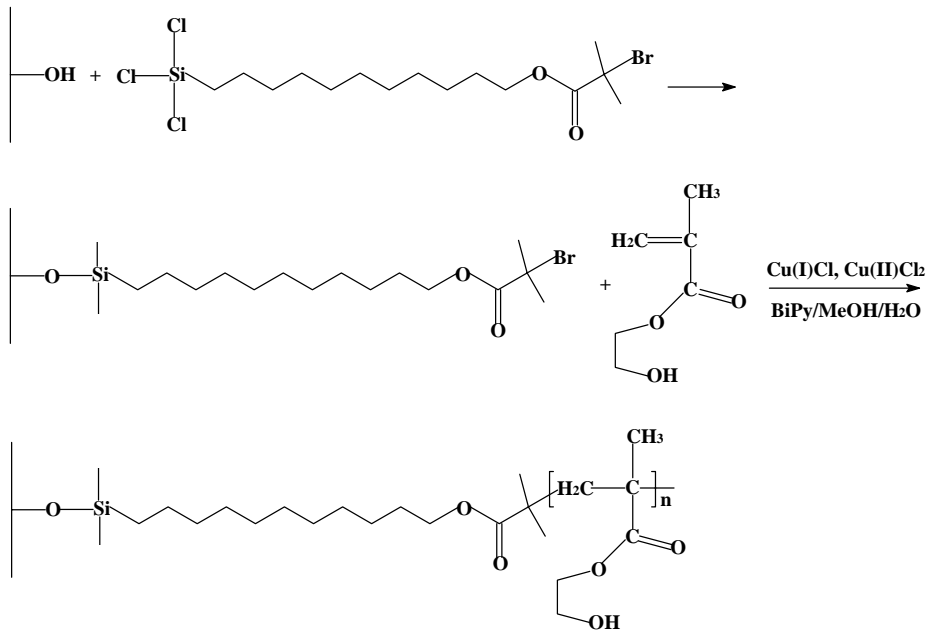
Key parameters that are expected to influence the efficiency of non-covalent attachment of molecules (here DNA) to sites in the polymer brush are the chain length (molecular weight) and grafting density (σ). In this vein, Jonson and Johansson conducted simulation studies indicating that an increase in molecular weight and grafting density would in turn cause an increase in particle adsorption between favorable polymer/particle interactions.²⁰ Recently, Bhat *et al* reported the use of polymer μ -gradient assemblies to tune the adhesion of cells.¹⁵ They were successful at designing a method of controlling and varying both the molecular weight and grafting density. In this chapter this technique is used to systematically evaluate the loading capacity of DNA in a polymer brush as a function of chain length. Methods will also be discussed that: (a) provide a synthetic route for oligonucleotide attachment to polymer brushes using less stringent conditions than

previously utilized and (b) reduce biological samples needed for evaluating polymer brush parameters in oligonucleotide attachment.

4.3 Results and Discussion

4.3.1 Surface Modification and Characterization

Here we utilize, atom transfer radical polymerization (ATRP) to produce a polymer backbone for DNA immobilization and hybridization. ATRP is an ideal technique because it provides molecular weight control. Although, as stated above, other polymers have been used to immobilize DNA, a systematic study of the effects of molecular weight has yet to be explored. To probe this, a surface tethered polymer gradient was synthesized via ATRP in which the molecular weight of the chains varied across the substrate. Poly (2-hydroxyethyl methacrylate) (PHEMA) was the polymer of choice because molecular weight of the polymer can be controlled using ATRP. In addition, the hydroxyl groups of PHEMA served as binding sites to a variety of functional groups.²¹ Scheme 4.2 outlines the synthetic route used to form a PHEMA brush as described by Tomlinson et al.²² The initiator (11-(2-bromo-2-methylpropionyloxy) undecyltrichlorosilane (BMPUS) was attached to the silicon substrate (the hydroxyl groups presented at the SiO₂/air interface are shown) via known trichlorosilane coupling chemistry. The tertiary bromide then acts as an ATRP initiation site when reacted with copper salts as shown in step two to ultimately produce a surface-attached polymer as shown in Step 2 of Scheme 4.2.



Scheme 4.2: Depicts the synthetic route to forming poly(hydroxyethyl methacrylate)

The polymer brush gradient provides a systematic variation in the length of the polymer chains across a single substrate. Moreover, an increase in the number of hydroxyl groups (which will subsequently be used as functional sites upon which to attach the DNA probe strands) will provide more sites for DNA immobilization.

To control the polymer chain length, a dipping apparatus (see experimental) was used. The chain length was determined by the amount of time the initiated substrate was exposed to the HEMA solution. Thus, the steepness of a gradient is dependent on the time of exposure as well. Although previous work has also explored variations in the initiator density and along a gradient, in the following experiments the density of initiator sites was kept constant to observe only the chain length effects on DNA immobilization.

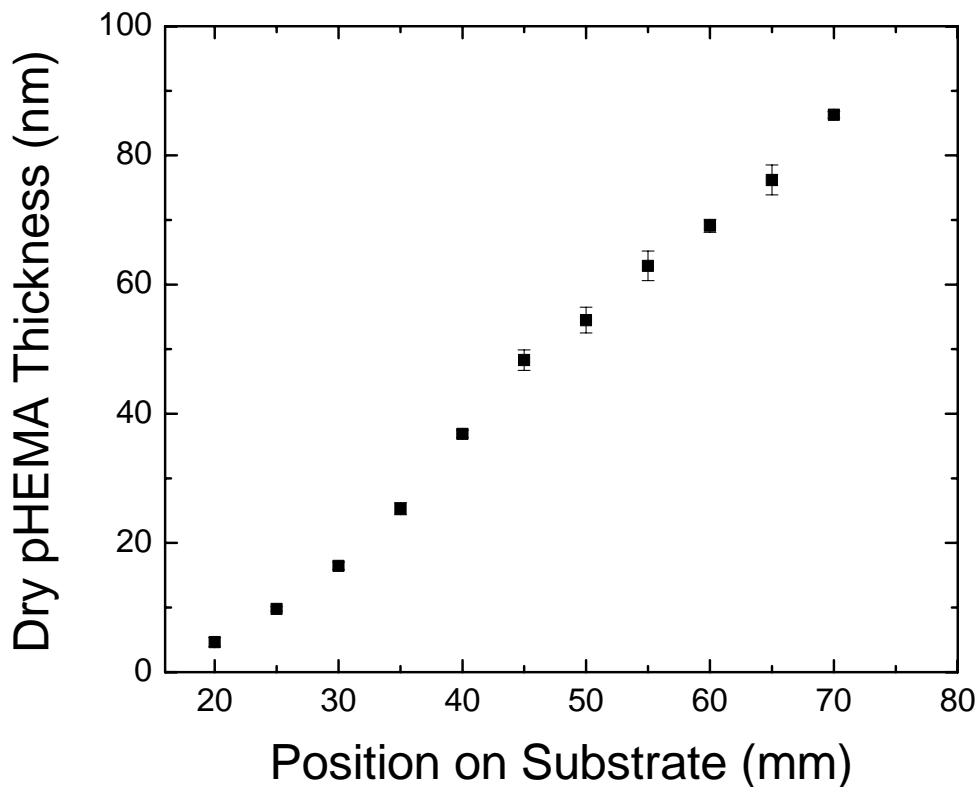
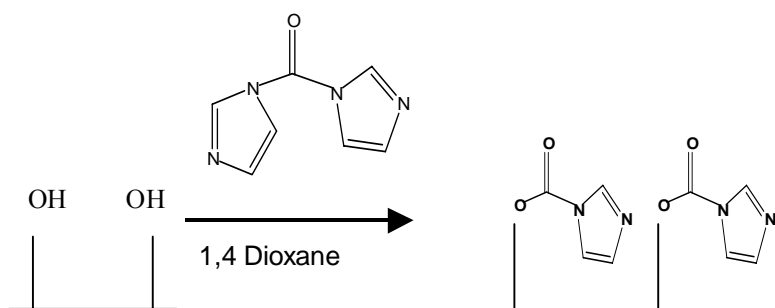


Figure 4.1: Provides the dry thickness polymer brush profile using ellipsometry across a silicon substrate corresponding to position and time.

Figure 4.1 shows the dry pHEMA thicknesses measured by ellipsometry at various positions along the substrate. The substrate was withdrawn from the polymerization solution at a rate of .04 mm/min. Thus, a relative position of zero indicates an exposure time of 0 minutes to the solution and a relative position of 70 mm indicates an exposure time of 1800 minutes to the solution. From the data, a systematic increase in thickness was observed as the length of time that the monomer solution was exposed to the surface-bound initiating

sites was increased. This graph indicates a molecular weight gradient of pHEMA has been formed along this substrate.

In order to modify the pHEMA brush gradient for DNA immobilization, the hydroxyl groups were converted to functional groups that could react with the amine terminus of a DNA oligomer. Various coupling agents have been described in the literature that have been used in similar chemistry. 1-ethyl-3-(3-dimethylaminopropyl) carbodiimide (EDAC)²³ and carbonyldiimidazole (CDI)²⁴ have both been utilized to “activate” the carboxyl and hydroxyl groups of polymer chains. CDI was an attractive coupling agent because the resulting ligand-polymer complex is stable and resists hydrolysis for extended periods of time. We utilized the CDI coupling technique to form an imidazolyl carbamate complex with the hydroxyl groups of the pHEMA brush gradient. The chemical steps showing the reaction of CDI with free hydroxyl groups on the pHEMA and the subsequent reaction with an amine are shown in Scheme 4.3.



Scheme 4.3 Schematic formation of carbonyldiimidazole attachment to the polymer brush backbone.

Fourier transform Infrared Spectroscopy (FT-IR) was used to monitor the coupling of CDI to pHEMA. IR spectra of the hydroxyl group stretching region (ca. 3400 cm^{-1}) of a pHEMA sample were obtained before (Figure 4.2a) and after two, six and twenty seven hours of immersion in a 0.2M solution of CDI (Figures 4.2b-d, respectively). The hydroxyl group stretching intensity decreased rapidly in the first two hours but no additional decrease was observed at longer incubation times. From these data, it is concluded that a two-hour incubation time was sufficient to maximize the conversion of the hydroxyl groups to carbonate groups. Notably, however, the hydroxyl group signal does not completely disappear. Water also absorbs in this region. Thus, these spectra might reflect the presence of adventitious water. It is thus not possible to conclude unambiguously whether reaction of the hydroxyl groups on the pHEMA was complete or only partial.

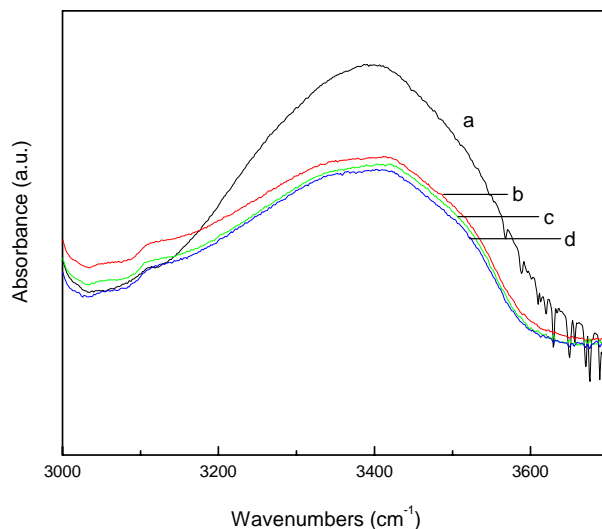
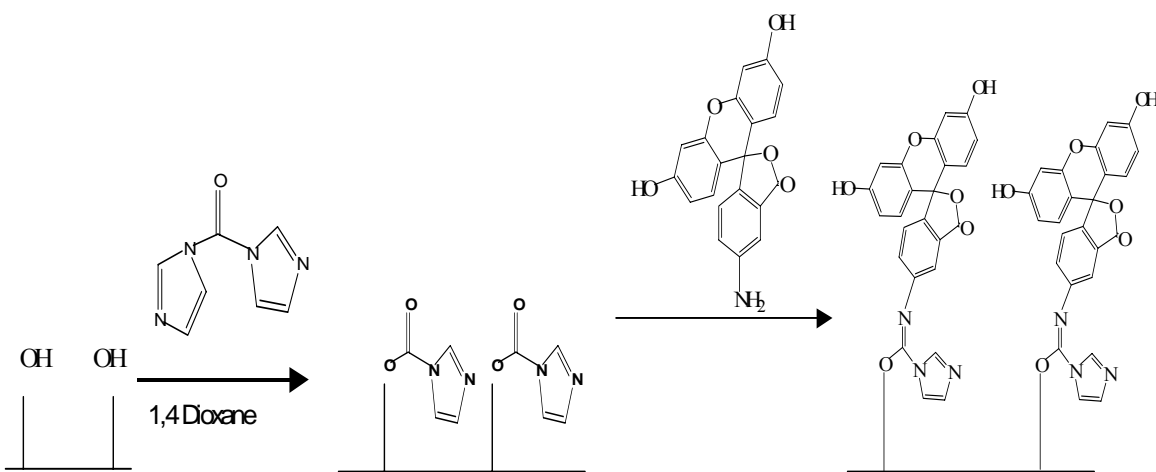


Figure 4.2: FT-IR spectra of hydroxy stretching region plotted as a function of time. Hydroxyl groups were monitored for pHEMA (a), pHEMA/CDI 2hrs (b), pHEMA/CDI 6hrs (c) and pHEMA/CDI 27hrs (d).

It was then of interest to investigate the reaction of an amine with the CDI-activated hydroxyl groups. Rather than using amine-terminated DNA as the initial probe, fluoresceinamine was employed first. Scheme 4.3 illustrates how fluoresceinamine was envisioned to couple to the CDI-activated polymer. Fluoresceinamine is comparable in size and fluorescence emission range to a fluorophore molecule that will be tethered to the DNA target probe in later experiments.



Scheme 4.3 Schematic formation of fluoresceinamine attachment to the polymer brush backbone.

In order to verify the presence of the immobilized fluoresceinamine probe FTIR was used to identify the addition of the amine groups. Figure 4.4 shows the FTIR spectra of pHEMA with the addition of fluoresceinamine for 6hrs. The presence of the amine group is

consistent with enhancement of the absorption peak in the 3500 - 3300 cm^{-1} range, corresponding to the N-H stretch.

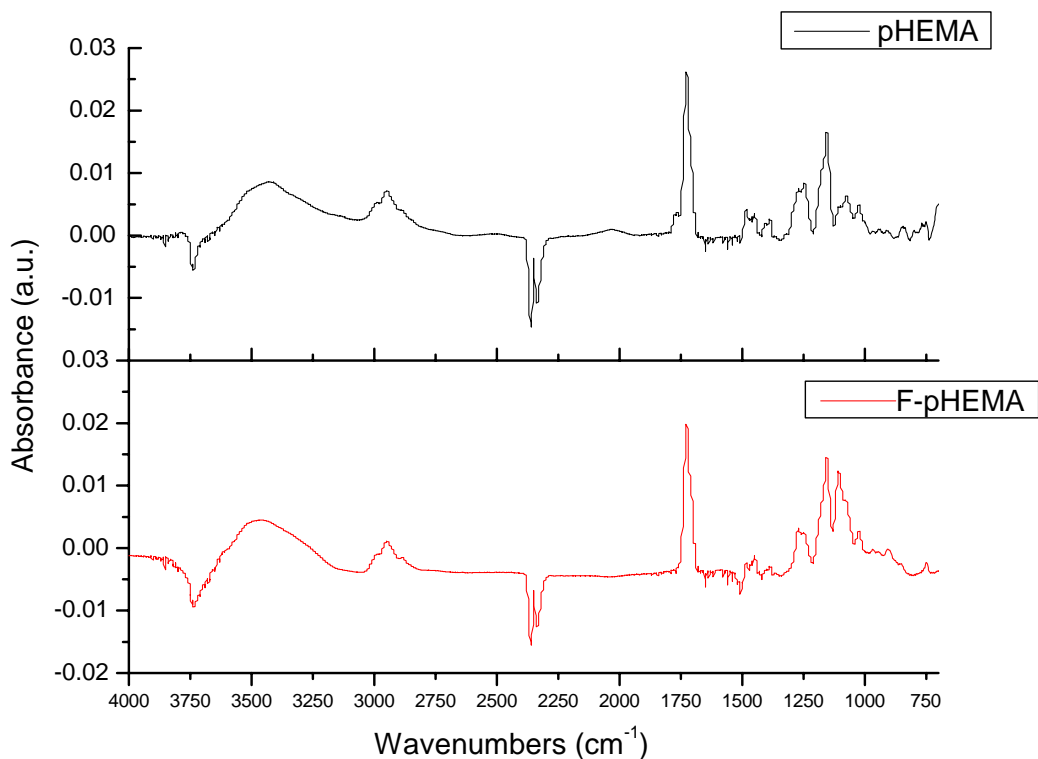


Figure 4.4: FTIR spectra of a pHEMA brush attached to a Si substrate before and after reaction with fluoresceinamine.

Next an “activated” polymer brush gradient was incubated in the fluorophore solution (.02M fluoresceinamine isomer I in phosphate buffer pH 7.4) for 1 hr. To determine the relative amount of fluoresceinamine that was incorporated at various positions along the gradient the presence of the fluoresceinamine probes were also confirmed by fluorescence microscopy. In Figure 4.5, the polymer thickness vs position profile is plotted along with

fluorescence intensity vs. position, for a single sample. The results indicate an increase in fluorescence intensity corresponding to an increase in polymer brush thickness.

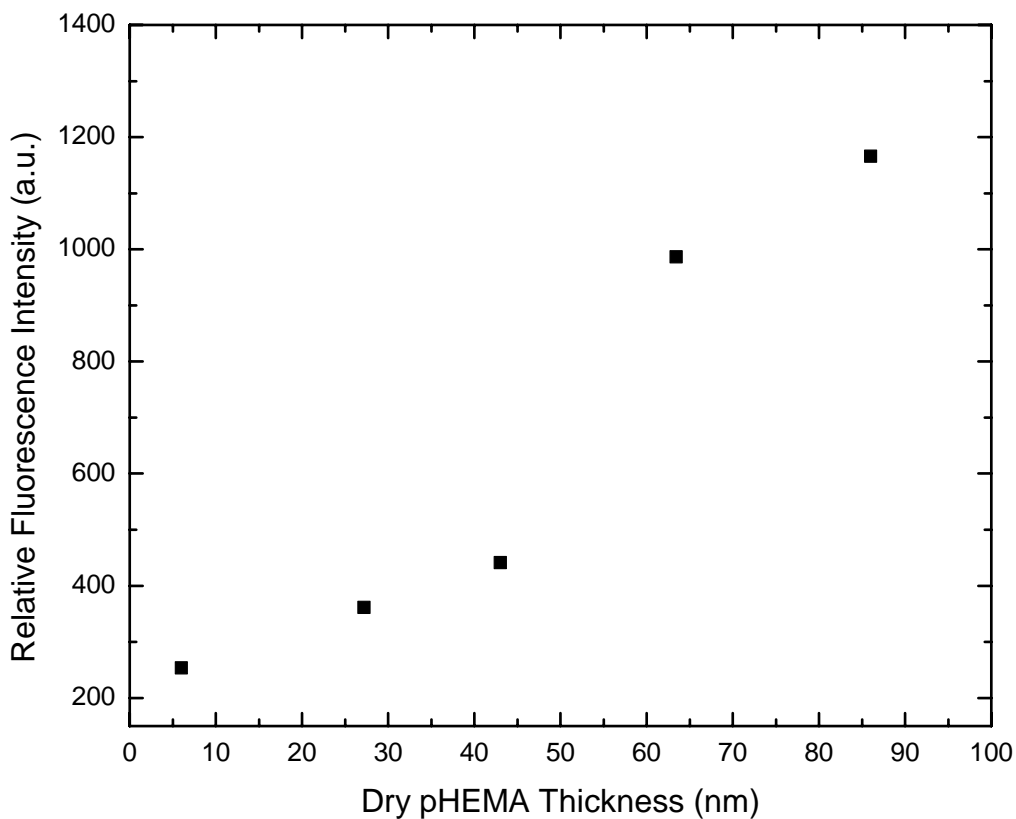


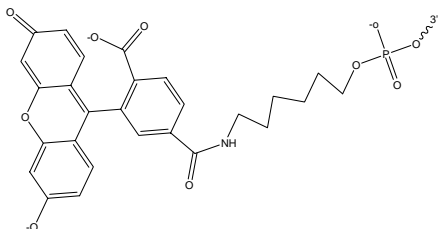
Figure 4.5: Graph showing fluorescence intensity vs. dry pHEMA thickness plot for fluoresceinamine attachment to a functionalized pHEMA gradient.

After successfully coupling the amine-terminated fluorophore to the pHEMA brush, the experiment was modified to incorporate single stranded DNA molecules containing amine end groups. The DNA sequences used here are listed in Table 4.1.

Table 4.1. List of DNA sequences

Name	Sequence
Amine Terminated Probe (DP)	5' -H ₂ N/TTG GAC TGT TAT CCG CTC ACA AT-3'
Complimentary (DC)	5' -FAM/ ATT GTG AGC GGA TAA CAG TCC AA-3'
Non Complimentary (DNC)	5' -FAM/ TTG GAC TGT TAT CCG CTC ACA AT-3'

Fluorophore: 5'-FAM*



The amine terminated probe (DP) contains an amine linkage that is used to couple with the imidazolyl carbamate complex sites along the polymer brush gradient. 50µL of capture probe solution were incubated on the activated polymer brush gradient for 6 hours (See experimental). This process was then followed by a 50 ml incubation of the detector probe (either complimentary or non complimentary) for 6hrs. The complimentary strand was a sequential match for hybridization of the amine terminated capture probe. In contrast, the non-complimentary strand served as a complete sequential mismatch for the amine terminated capture probe. Single strands of DNA that were alternatively complimentary and

* FAM- 6-carboxyfluorescein is a single isomer derivative of fluorescein

non complimentary to the immobilized single strand were used as detection probes to determine the hybridization efficiency with the amine terminated probe. Both detection probes contained the fluorophore 5-carboxyfluorescein (5-FAM) to identify their presence after incubation with the substrate. In the case of the complementary strand, the presence of this fluorophore could be taken as an indication of hybridization between the two strands. In the case of the non-complementary strand, the presence of this fluorophore could be taken as an indication of non-specific binding between the strand and the sample.

Figure 4.6 shows fluorescence images of unreacted pHEMA without any DNA present, and three regions of DNA hybridization along the polymer brush gradient. Green fluorescence emission was observed upon attachment of 5'FAM labeled complimentary DNA to the pHEMA gradient surface with amine terminated DNA strands. There was no detectable fluorescence emission observed in the case of a non-reacted pHEMA surface (Figure 4.6a). The images indicate a decrease in fluorescence emission as the polymer brush thickness decreases. The images show an increase in fluorescence intensity as the polymer brush thickness increases.

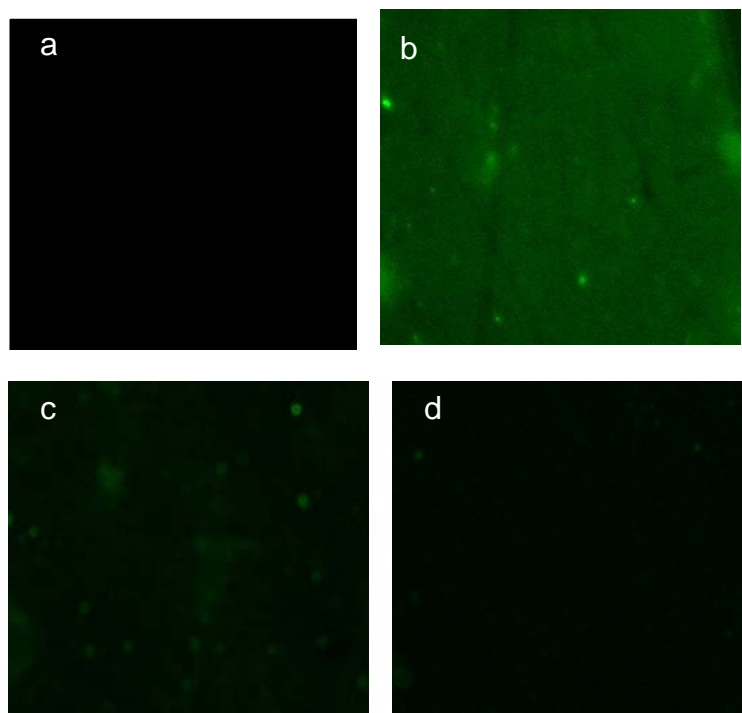


Figure 4.6: Fluorescence micrographs (top) and corresponding intensity depicts a.unreacted pHEMA and b-d pHEMA after grafting with DNA probe and complimentary strand via CDI coupling for 63.5 (nm), 37.0 (nm), 21.3 (nm). Images were collected using 20x magnification.

In Figure 4.7, the relative fluorescence intensity is plotted versus the thickness of the pHEMA polymer brush across the thickness gradient. When the complimentary DNA strand was incubated with the polymer containing the capture strands, an increase in fluorescence intensity was observed as the pHEMA brush thickness increases. This increase was similar to that observed in the experiment conducted with fluoresceinamine. In contrast, the fluorescence emission in the presence of the non-complementary DNA probe was consistently lower than that observed with the complimentary DNA strand. Furthermore, the magnitude of the fluorescence was not affected by change in the dry pHEMA brush

thickness. In Figure 4.7 the 0mm position indicates the background, thus the background is similar to that measured in the presence of the non-complementary strand.

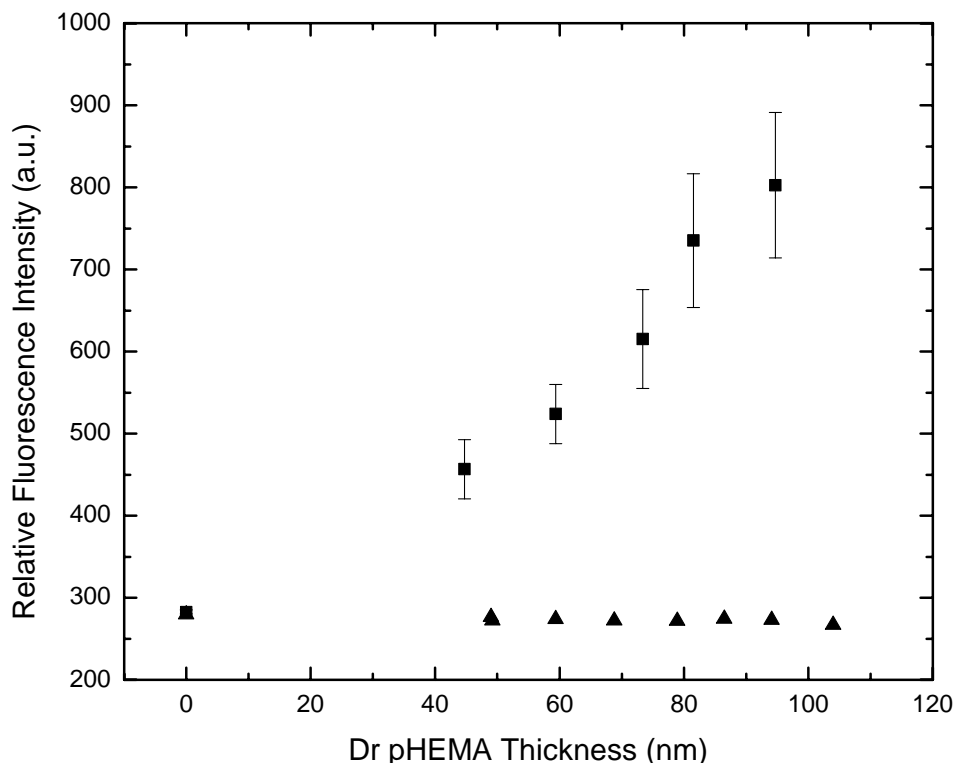


Figure 4.7: Graph shows fluorescence intensity vs. polymer thickness data for hybridization of complimentary (■) and non-complimentary (▲) DNA on target DNA modified polymer gradient. The single data point at zero. Dry pHEMA thickness indicates the Background for both samples.

In order to collect additional information on DNA immobilization within the polymer brush particle based experiments were conducted. Gold nanoparticles (13nm) precoated with 23-mer amine-terminated single strand DNA (in deionized water) were synthesized (ref X.Lou). The nanoparticle solution was spotted along the CDI functionalized pHEMA

gradient and allowed to sit for 6 hrs at room temperature. Glass cover slips were used for even distribution. The substrates were then rinsed with deionized water and dried under a nitrogen stream. Atomic force microscopy was then used to analyze the substrate (Figure 4.8). The results indicate a higher nanoparticle concentration in the polymer brush range (22-38 nm) and a considerable decrease in nanoparticle concentration in the thicker polymer brush range (60-74 nm). In correlation with the previous DNA hybridization data conducted on a pHEMA gradient, it is reported that the fluorescence intensity increases with increasing polymer brush thickness. Thus, it was expected that the particle-based experiments imply fluorescence intensity would be higher in the thicker polymer brush region where fewer nanoparticles were observed. Because the AFM images were measured using the tapping mode on the surface of the substrate, this could possibly suggest that the nanoparticles were embedded within the longer chain length polymer brush. This would also support the hypothesis that as you increase the polymer brush thickness at a fixed grafting density, there are more functional sites along the polymer brush that can be used for DNA immobilization. However this data may reflect fewer nanoparticles were observed on the thicker polymer film compared to those on thinner polymer film could be due to a steric effect. The reactive sites underneath the surface may not have been accessible to the nanoparticles for the high molecular weight surface that more densely packed compared to the low molecular surface. For the case of ssDNA, the small size of ssDNA allows for accessibility to the area beneath the surface. This was verified via fluorescence imaging.

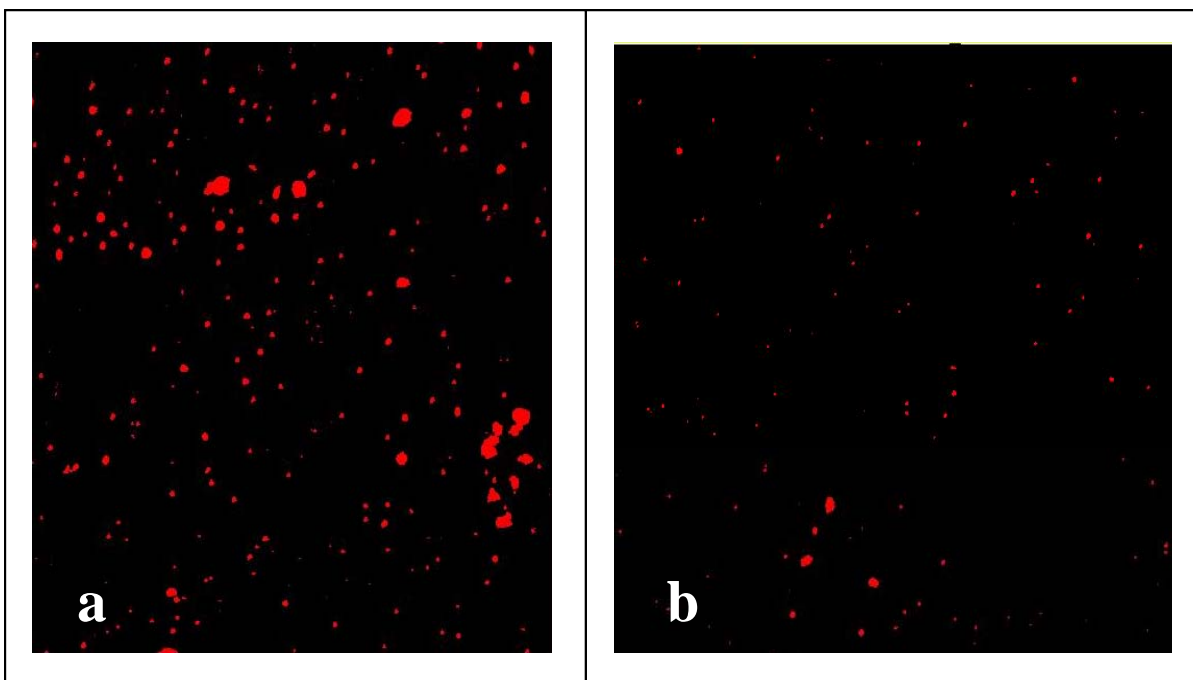


Figure 4.8: Atomic force microscopy images DNA coated Gold nanoparticles in a low (22-38nm) and high molecular weight polymer brush (62-74nm). In the low molecular weight regime the density of particles is $18.205 \mu\text{m}^3$ vs that of the high molecular weight regime of $7.843 \mu\text{m}^3$.

4.4 Conclusions

An efficient method of systematically varying the chain length of a polymer brush on a single substrate for DNA immobilization and hybridization has been reported in this chapter. We concluded as the polymer brush increased, an increase in fluorescence intensity was observed. Atom transfer radical polymerization provided a controlled synthetic route for the polymer brush platform using milder conditions than previously reported. The polymer brush gradient provided DNA immobilization data on a single substrate that indicated an increase

in chain length at a fixed grafting density, can provide an increase in access sites along the polymer brush capable of DNA attachment and immobilization.

4.5 Implementation / Experimental

4.5.1 Materials

Silicon Wafers (Sb-doped, 0.01-0.02ohm-cm) were purchased from Silicon Valley Microelectronics. 2-Hydroxyethyl methacrylate (HEMA), CuCl, CuCl₂, 2,2'-bipyridine, 1'-carbonyldiimidazole (CDI), N-hydroxysuccinimide (NHS), triethylamine (TEA) were purchased (Sigma Aldrich, St.Louis, MO) and used as received without further purification. Oligonucleotides were purchased from Integrated DNA Technologies (Coralville, IA). DNA sequences are listed in Table 4.1.

4.5.2 ATRP Synthesis of Surface- Initiated Polymerization Gradient

Polymer films were prepared via atom transfer radical polymerization. Hydrolyzed silicon wafers were prepared by exposing the wafers to ultraviolet ozone light (Ultraviolet Ozone Chamber Model 42, Jelight Company, Inc) for 10minutes. The Si wafer was then immersed in 30mL of chilled toluene. 20μL of 11-(2-bromo-2-methylpropionyloxy) undecyltrichlorosilane (BMPUS) was added to the immersed wafer and the solution then chilled for 24 hours. The modified silicon wafer was then sonicated in fresh toluene for 20 minutes and dried with N₂. This step was repeated 3 times to thoroughly remove physisorbed initiator. The dipping apparatus developed by the Genzer Group (Tomlinson, M.) was used under nitrogen purge (Figure 4.9). The apparatus was programmed to insert the initiator

covered silicon wafer into a mixture of HEMA, CuCl, CuCl₂, bipy, methanol, and water solution at a rate of 0.01mm per 15 seconds. The reaction time was dependent on the desired thickness. The PHEMA-modified sample was then sonicated in methanol and water for 20 minutes. The dry PHEMA gradient was then characterized using ellipsometry (Rudolf Auto el) to determine the PHEMA gradient thickness along the substrate. The results of the position along the substrate vs. dry pHEMA thickness are shown in Figure 4.1.

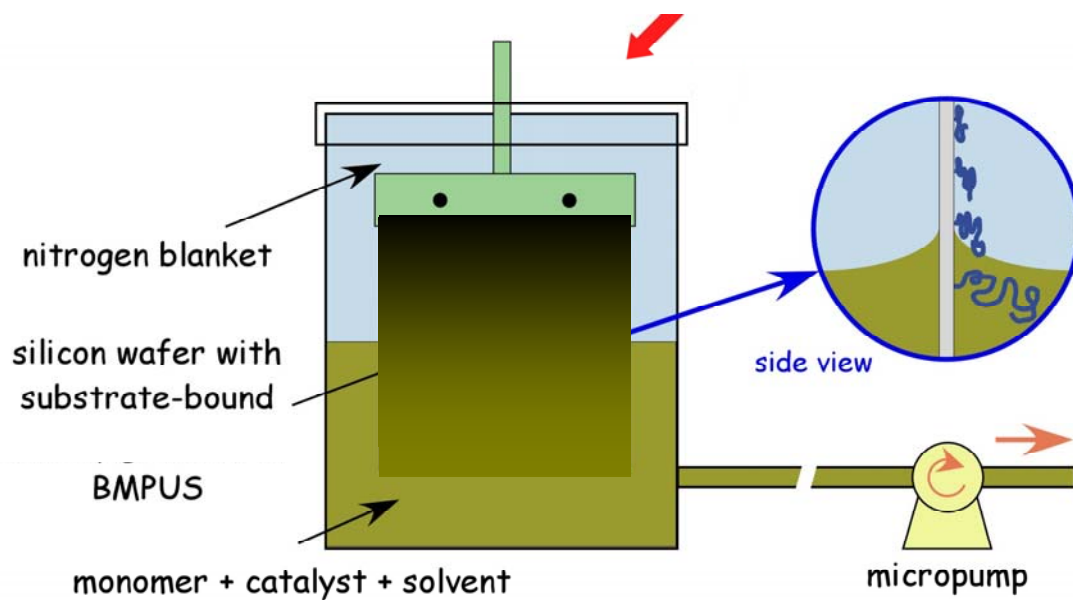


Figure 4.9: Illustrates the apparatus designed to systematically vary molecular weight and or grafting density on a substrate (Illustration courtesy of J. Genzer)

4.5.3 Covalent Coupling via 1, 1' Carbonyldiimidazole (CDI) reaction

To functionalize the PHEMA gradient, the coated substrate was immersed in freshly prepared 0.20 M 1,4 Carbonyldiimidazole in 1,4 Dioxane for 24 hrs at room temperature. Carbonyldiimidazole activates hydroxyls present in the polymer film and enables subsequent reaction with amine-containing species. The coated substrate was sonicated in 1,4 dioxane three times and dried with a flow of nitrogen. Figure 2 shows the successful coupling of the polymer solution upon the addition on CDI by monitoring the hydroxyl groups using FTIR.

4.5.4 Capture Probe Immobilization and DNA Hybridization

DNA capture probe (CP) solutions were coupled onto the polymer surface by incubating 1 μ M CP in NaHCO₃ / Na CO₃ (0.1M, pH 9) buffer solution on the CDI-functionalized polymeric substrate. Cover slip glass slides were used to evenly spread the DNA solution along the functionalized polymeric substrate in a sandwich assembly. After 6 hours at room temperature, the samples were removed and followed by rinsing of a solution of TE (Tris EDTA) buffer and dried with nitrogen.

For hybridization, the aforementioned procedure was again used to incubate the fluorescent-labeled DNA complimentary (c) or noncomplimentary (nc) strand with the capture probe coated polymer surface. 50 μ L of target oligonucleotides (c or nc) were prepared with a 1M solution of NaCl TE (tris EDTA) buffer. During hybridization extra

caution was used to minimize the exposure to light. After hybridization, the completed pHEMA gradient (with fluorophore hybridization) was then rinsed with the TE buffer and deionized water.

4.5 Instrumentation

Film thickness measurements were obtained using the Rudolph Auto el instrument. An incident angle of 70° was used to irradiate the substrate. A refractive index of 1.51 was used to measure pHEMA thickness along the substrate.

Interfacial tension behavior data of the pHEMA vs DNA immobilized pHEMA was detected using goniometry. A Ramehart optical goniometer was used to collect measurements. Triplicates of each contact angle position were collected and individually fit to the Young/ Laplace model. The changes in contact angle measurements reflect the differences in surface chemistry during the sequential steps of DNA hybridization on polymer surfaces. After polymerization on a single substrate (64nm) a measured contact angle of ($\sim 47^\circ$) was observed. Upon CDI coupling, less polar functional groups were being added to the surface, which caused an increase in the contact angle. This is reflected in the increase in contact angle measurements collected after CDI coupling ($\sim 70^\circ$). DNA is negatively charged and upon interaction with a surface this caused a significant decrease in contact angle to ($\sim 34^\circ$). At the onset of DNA hybridization, the contact angle decreases at varying polymer thickness.

Reflectance FT-IR was collected using the Bio Rad Model FTIR Spectrometer equipped with a PIKE attachment. The reflectance mode provided a spectral resolution of 4cm^{-1} at 256 scans using a mercury cadmium telluride (MCT) detector. FTIR was used to monitor the sequential steps: polymer formation, cdi coupling and DNA attachment.

A digitally enhanced fluorescent microscope was used to quantify the amount of DNA bound to the PHEMA gradient. A Zeiss Axioplan 2 setup was used with the Sutter Instrument Corp. It includes a Xe fiber optic arc lamp, a fluorescent filter set #38 HE from Zeiss with bandpasses at $470\text{nm} \pm 40\text{nm}$ for excitation and $525\text{nm} \pm 50\text{nm}$ for emission, a LEP LudL BioPoint 2 motorized stage and a Hamamatsu Orca-ER Digital Camera. The software interface with the microscope was Andor iQ (Andor Technology). The two primary reasons for using a fluorescent microscopy setup were 1) automation and precision control using programmable scans with the LudL automated stage and 2) detection sensitivity and image quality that are comparable to any fluorometer available to us. Images were taken using a Zeiss 20X Plan-NEOFLUAR objective with $\text{NA} = 0.50$.

EN.REFLIST

4.6 References

- (1) Pirrung, M. *Angew. Chem. Int. Ed.* **2002**, *41*, 1276-1289.
- (2) Devaux, C., Chapel, J.P.; Beyou, E.; Chaumont, P. *Eur. Phys. J. E* **2002**, *7*, 345-35.
- (3) Pirri, G.; Chiari, M.; Damin, F.; Meo, A. *Anal. Chem.* **2006**, *78*, 3118-3124.
- (4) Gong, P.; Grainger, D. *Surface Science* **2004**, *570*, 67-77.
- (5) Steel, A.; Herne, T.; Tarlov, M. *Anal. Chem.* **1998**, *70*, 4670-4677.
- (6) Hong, B.; Oh, S.; Youn, T.; Kwon, S.; Park, J. *Langmuir* **2005**, *21*, 4257-4261.
- (7) Swami, N.; C., C.-F.; Terberueggen, R. *Langmuir* **2005**, *21*, 1937-1941.
- (8) Vandenberg, E.; Bertilsson, L.; Leidberg, B.; Uvdal, K.; Erlandson, R.; Elwing, H.; Lundstrom, I. *J. Colloid Interface Sci.* **1991**, *147*, 103-118.
- (9) Benters, R.; Niemeyer, C. M.; Drutschmann, D.; Blohm, D.; Wohrle, D. *Nucleic Acids Research*, **2002**, *30*
- (10) Edmondson, S.; Osborne, V.; Huck, W. *Chem. Soc. Rev* **2004**, *33*, 14-22.
- (11) Lenigk, R.; Carles, M.; Ip, N.; Sucher, N. *Langmuir*, **2001**, *17*, 2497
- (12) Smith, E.; Wanat, M.; Cheng, Y.; Barreira, S.; Fritos, A.; Corn, R. *Langmuir*, **2001**, *17*, 2502
- (13) Oh, S.; Cho, S.; Kim, C.; Park, J. *Langmuir*, **2002**, *18*, 1764
- (14) Strother, T.; Chai, W.; Zhao, X.; Hamers, R.; Smith, L. *J. Am. Chem. Soc.*, **2000**, *122*, 1205
- (15) Bhat, R.; Chaney, B.; Rowley, C.; Liebmann-Vinson, A.; Genzer, J. *Adv. Mat.* **2005**, *17*, 2802-2807

- (16) Aksay, A.; Trau, M.; Manne, S.; Honma, I.; Yao, N.; Zhou, L.; Fenter, P.; Eisenberger, P.; Gruner, S. *Science*, **1996**, 273, 892-894
- (17) Mansky, P.; Liu, Y.; Huang, E.; Russell, T.; Hawker, C. *Science* **1997**, 275, 1458
- (18) Klein, J.; Kumacheva, E.; Mahalu, D.; Perahia, D.; Fetters, L. *Nature* **1994**, 370, 634.
- (19) Kai, Q.; Vhuanzhen, Z.; Walker, A.; Wooley, K.; Jhaveri, S.; Sogah, D.; Malkoch, M.; Beinhoff, M.; Carter, K.; Hawker, C. *Polymer Preprints* **2005**, 46, 363.
- (20) Jonsson, M.; Johansson, O. *Colloids Surf. B.* **2004**, 37.
- (21) Huang, W.; Kim, J.; Bruening, M.; Baker, G. *Macromolecules* **2002**, 35, 1175-1179.
- (22) Tomlinson, M. Genzer, J. *Macromolecules* **2003**, 36, 3449
- (23) Staros, J.; Wright, R.; Swingle, D. *Analy. Bio.* **1986**, 156, 220-222
- (24) McArthur, S.; Halter, M.; Vogel, V.; Castner, D. *Langmuir*, **2003**, 19, 8316-8324

Chapter 5: Controllable Nano Patterned Polar Surfaces for Molecular Pattern Formation and Transfer

5.1 Project Goals and Motivation

In recent years it has become possible to control the charge distribution of a surface at the micron, or smaller length scales.¹ The fabrication of periodically charged domains on a substrate has sparked a demand in research areas across scientific disciplines such as physics, chemistry, engineering and even nano-technology.² Interdisciplinary collaborations have led to technological advances in computer memory, infrared sensors and medical ultrasound detectors.^{3,4}

Ferroelectrics are a class of materials that have been used in switchable poling applications that require sizes down to the nanometric range.³ Ferroelectric materials are characterized by spontaneous polarization, which can be changed by applying an electrical field. In order to fabricate nanosized domains using ferroelectric materials, creative methods such as lithography-based patterning techniques, the use of nanoelectrodes, and even microemulsion techniques have been explored.^{3,5}

In this chapter, self-assembly of polar molecules will be used as a paradigm for nano-scale construction on a periodically poled substrate. Our goal is to show that electrostatic interactions between a polarized ferroelectric domain and polar molecules can be a new way to drive self-assembly that is amenable to patterning. To achieve this goal we plan to establish the molecular features required to self-assemble on a polarized ferroelectric domain. We will then assemble and characterize these molecules on polarized, patterned

ferroelectric substrates with well-controlled surfaces. We believe the electrostatic interaction between a poled surface and polar molecule can lead to advancement in nano printing and molecular dynamics.

5.2 Introduction:

5.2.1 Ferroelectric Materials:

Substantial research and development has been devoted to ferroelectric materials such as single ionic crystals, piezoelectric polymers, composites and thin films.^{2,4} Ferroelectrics can be used as capacitors, optoelectronic devices and actuators.^{3,6-8} These materials are unique because they all exhibit a spontaneous dipole moment, which can be reversed by the application of an electric field.

There are two main types of ferroelectric materials: order-disorder and displacive.^{9,10} In an order-disorder ferroelectrics, there is a dipole moment in each unit cell, but at high temperatures the dipoles are pointing in random directions. Lowering the temperature induces a phase transition that causes the dipoles to order and all point in the same direction within a domain. Displacive behavior arises from an asymmetrical shift in the equilibrium ion positions causing a permanent dipole moment.

Lithium Niobate is a widely used ferroelectric material because of its unique electro-optical, photoelastic, piezoelectric and non-linear properties.¹¹ LiNbO_3 was used in our studies because of its availability, reasonable price and its capability of domain reversal via periodic poling.¹² The attractiveness of periodic poled lithium niobate (PPLN) lies in the ease

with which the size, distribution, and periodicity of its ferroelectric domain can be engineered to match the requirements of a given application.

Patterned domain reversal in lithium niobate has been extensively investigated using a wide number of treatments involving heat, chemical, and electric field poling techniques.¹² The most commonly used method of poling LiNbO_3 was discovered by Yamada *et al.* in 1993.¹³ They discovered that lithium niobate could be poled by patterning electrodes onto the surface of a substrate and applying a large electric field. In domains directly underneath the electrodes, the internal electric field changed sign, and these domains propagated through the crystal with minimal lateral spreading. The basic structure of a PPLN crystal is shown in Fig. 5.1, which illustrates the periodic variation of the internal electric field along its length.

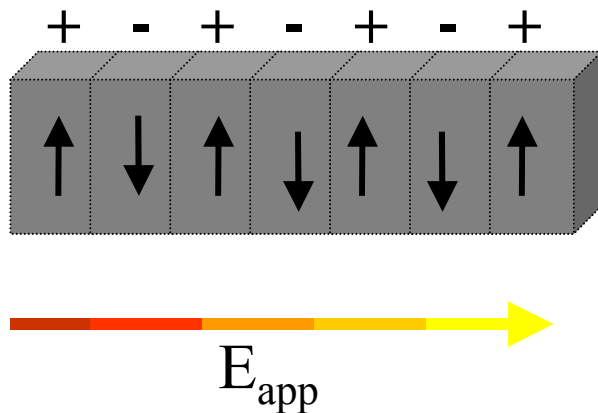


Figure 5.1: Illustration is shown of the domain directions of a periodically poled lithium niobate. The E_{app} arrow indicates the direction in which the electric field is applied.

5.2.2 Self Assembly of Polar Molecules

Self-assembled monolayers of various organic molecules can be used to modify the surface chemistry of complex metal oxides.³ The self-assembly of molecules onto a surface is a flexible technique that can be used to specifically tailor molecule / substrate interactions. The molecules used in self-assembly can create interfaces with desired structures and properties on various substrates. Self-assembly of surface bound molecules can impact a broad range of physical phenomena from a single molecular switch to functional optoelectronic materials. In this chapter the goal is to use electrostatic interactions between oppositely charged molecules and poled substrates to form a two-dimensional ordered molecular assembly.

5.3 Results and Discussion

In order to successfully achieve electrostatic interactions between charged molecules and a periodically poled surface, we devised the three-step plan shown in Scheme 1. The steps include 1) cleaning and passivation of the lithium niobate, 2) deposition of the charged molecules onto the poled lithium niobate surface, and 3) characterization of the chemically modified poled substrate. Each step will be discussed in detail in the following sections.

deposition was conducted by immersing the lithium niobate into a 13 mM solution of bromoacetic acid in H₂O for 30 seconds.

X-ray Photoelectron Spectroscopy (XPS) was then used for chemical analysis of the modified lithium niobate. In the presence of bromine, XPS spectra should show a peak at ~70 eV.¹⁵ XPS measurements were taken before and after immersion of the poled lithium niobate in bromoacetic acid. The XPS data did not reflect a significant distinction in peak intensity between the bromine positive and negative binding energy of the charged surface of lithium niobate.

It was hypothesized that the polar solvent used in conjunction with the bromoacetic acid solution deposition screens the charge, lowering the impetus for electrostatic assembly. To attempt to avoid this problem, a vapor deposition method was employed. The bromoacetic acid was melted in a chamber at 100° C. The melted bromoacetic acid was sealed in a vacuum chamber and vacuum was pulled. The vacuum chamber provided dry conditions to minimize outside moisture.

XPS was then immediately used to detect change in the intensity of the bromine adsorption to the poled lithium niobate surfaces. The results from vapor deposition of bromoacetic acid on poled lithium niobate samples are shown in Figure 5.2-4. In Figure 5.2 the vapor chamber containing lithium niobate and bromoacetic acid was heated to 120°C at 60 torr vapor pressure. The bromoacetic acid vapors were allowed to chemisorb onto the lithium niobate sample under vacuum for 1.5 hours. The Br to Nb signals indicate a ca. 10-fold preference for the positive side of the sample compared to the negative side of the sample.

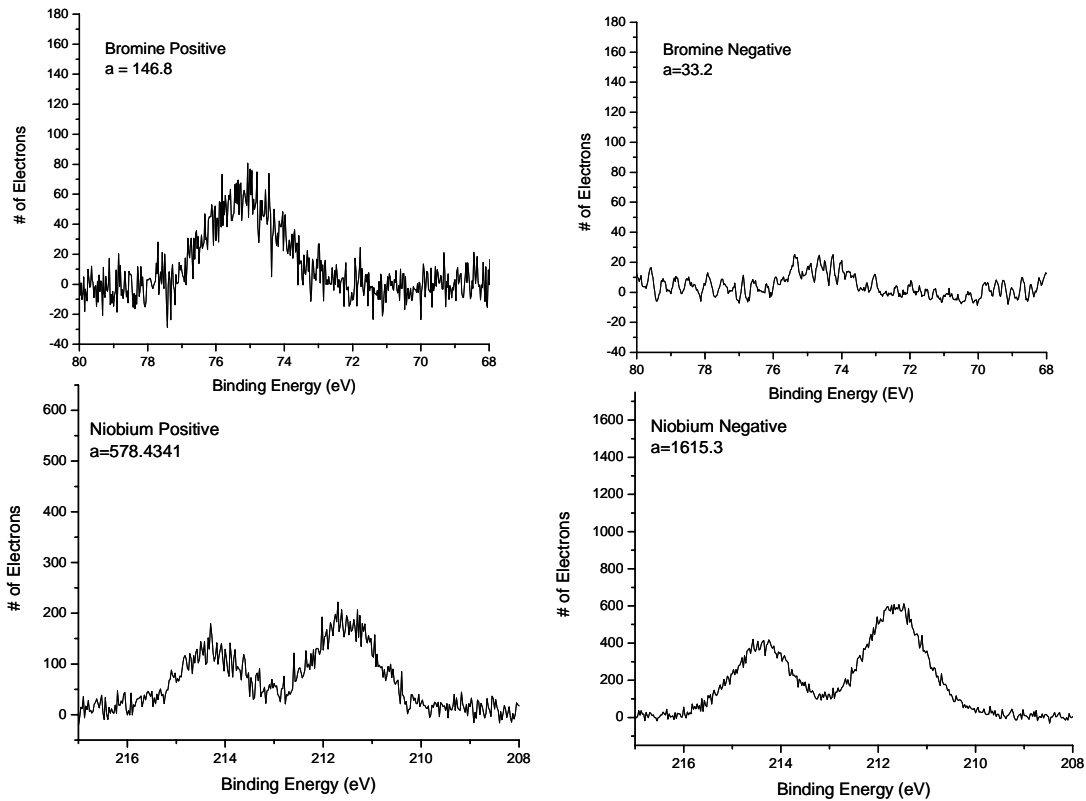


Figure 5.2: X-ray photoelectron spectra at a takeoff angle of 90° of poled lithium niobate positively and negatively charged surfaces after vapor phase exposure to bromo acetic acid ($\text{Br}_2\text{CH}_2\text{CO}_2\text{H}$). Representative peaks of Nb and Br are indicated. The $\text{Br}_2\text{CH}_2\text{CO}_2\text{H}$ self assembled monolayer was formed under the following conditions (temperature 120°C , vapor pressure 60 torr for 1hr). The Br/Nb (+) / Br/Nb (-) intensity ratio was 3.9 to 1.

Figure 5.3 shows the results of doubling the deposition time to 3 hours to observe the effects of Br saturation on the lithium niobate. The results indicate an increase in bromine molecules detected and a higher intensity of bromine binding to the positive side of the poled lithium niobate.

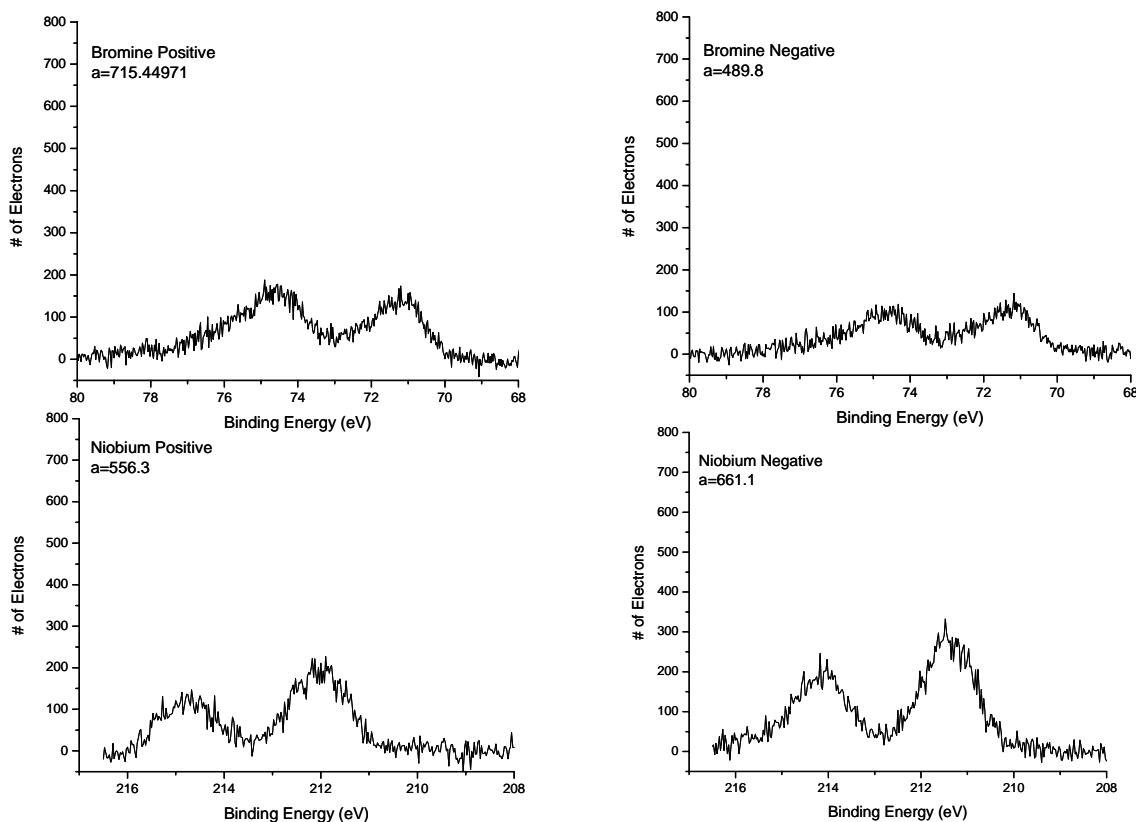


Figure 5.3: X-ray photoelectron spectra at a takeoff angle of 90° of poled lithium niobate positively and negatively charged surfaces after vapor phase exposure to bromo acetic acid ($\text{Br}_2\text{CH}_2\text{CO}_2\text{H}$). The $\text{Br}_2\text{CH}_2\text{CO}_2\text{H}$ self assembled monolayer was formed under the following conditions (temperature 120°C , vapor pressure 54 torr for 1.5 hr). Representative peaks of Nb and Br are indicated. The Br/Nb (+) / Br/Nb (-) intensity ratio was .749/. 45.

The deposition time was then lowered to 1 hr with an increase in vacuum pressure to 105 torr and the results are provided in Figure 5.4. The results continued to demonstrate an increase in relative bromine intensity to the lithium niobate.

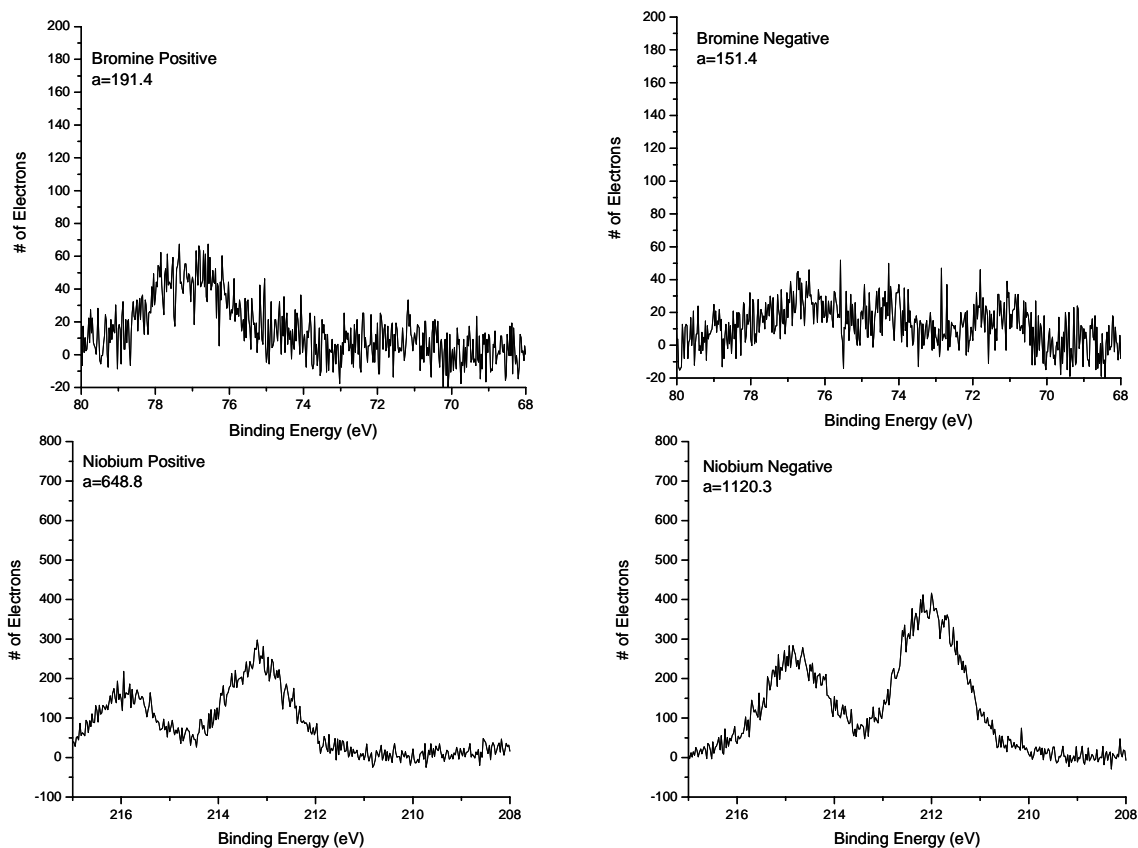


Figure 5.4: X-ray photoelectron spectra at a takeoff angle of 90° of poled lithium niobate positively and negatively charged surfaces after vapor phase exposure to bromo acetic acid ($\text{Br}_2\text{CH}_2\text{CO}_2\text{H}$). Representative peaks of Nb and Br are indicated. The $\text{Br}_2\text{CH}_2\text{CO}_2\text{H}$ self assembled monolayer was formed under the following conditions (temperature 100°C , vapor pressure 54 torr for .5 hr). The Br/Nb (+) / Br/Nb (-) intensity ratio was .295/. 137.

The results from each spectrum are consistent with electrostatic binding if the bromoacetic acid reversibly protonating the surface hydroxyls of the lithium niobate, providing a negatively charged carboxylate.

5.3.2 Periodic Poled Lithium Niobate (PPLN)

The next step was to determine if the selective binding behavior of bromine molecules to the lithium niobate surface could be observed on periodically poled domains on a single face of lithium niobate. Samples with micron-sized structures patterned on lithium niobate were obtained from the Nemanich group (Figure 5.5). The diagram shows the regions of periodic poling along the lithium niobate substrate.

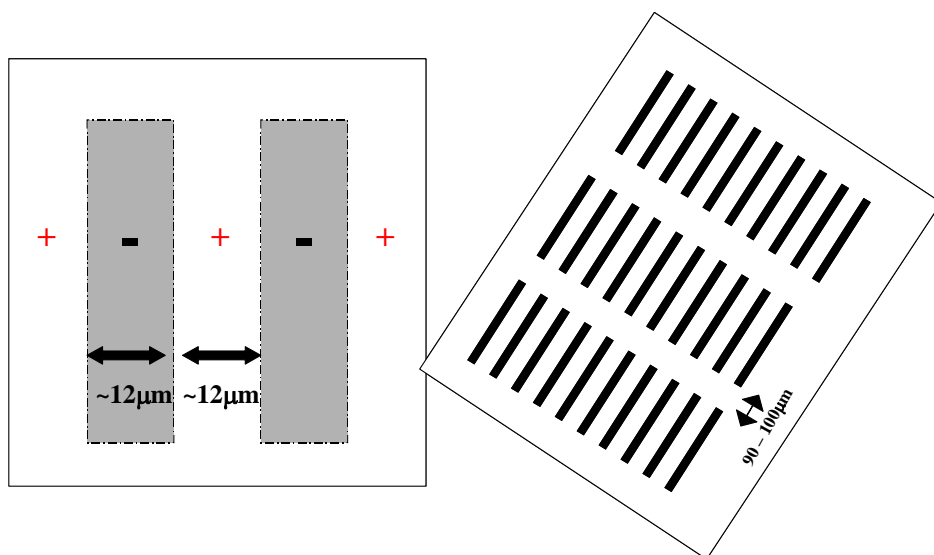


Figure 5.5: Diagram of periodic poled LiNbO₃ as purchased. Illustration (left) indicates the spacing and charge between each periodically poled domain. The right illustration provides the aerial view of the entire periodically poled sample on a single lithium niobate surface.

The procedure for passivation using TMSCl and vapor deposition of bromoacetic acid was carried out as previously described. An initial attempt was made to characterize the brominated PPLN surface with elemental mapping using an EDS detector scanning electron

microscopy. The poor results from the images indicated the information depth of the instrument was much larger than the deposit layer thickness.

Time of Flight Secondary Ion Mass Spectrometry (TOF-SIMS) was then used as a characterization technique to give elemental composition maps with higher spectral resolution and surface sensitivity in the nanometric size scale. Figures 5.6-8 represent the images retrieved from the TOF-SIMS data. Figure 5.6 depicts negative ion scanning images of the PPLN sample. A contoured pattern is noticed in the elemental mapping of Br, b. CH, c. H, and d. OH. The contours are consistent in size with the patterned domains of the PPLN.

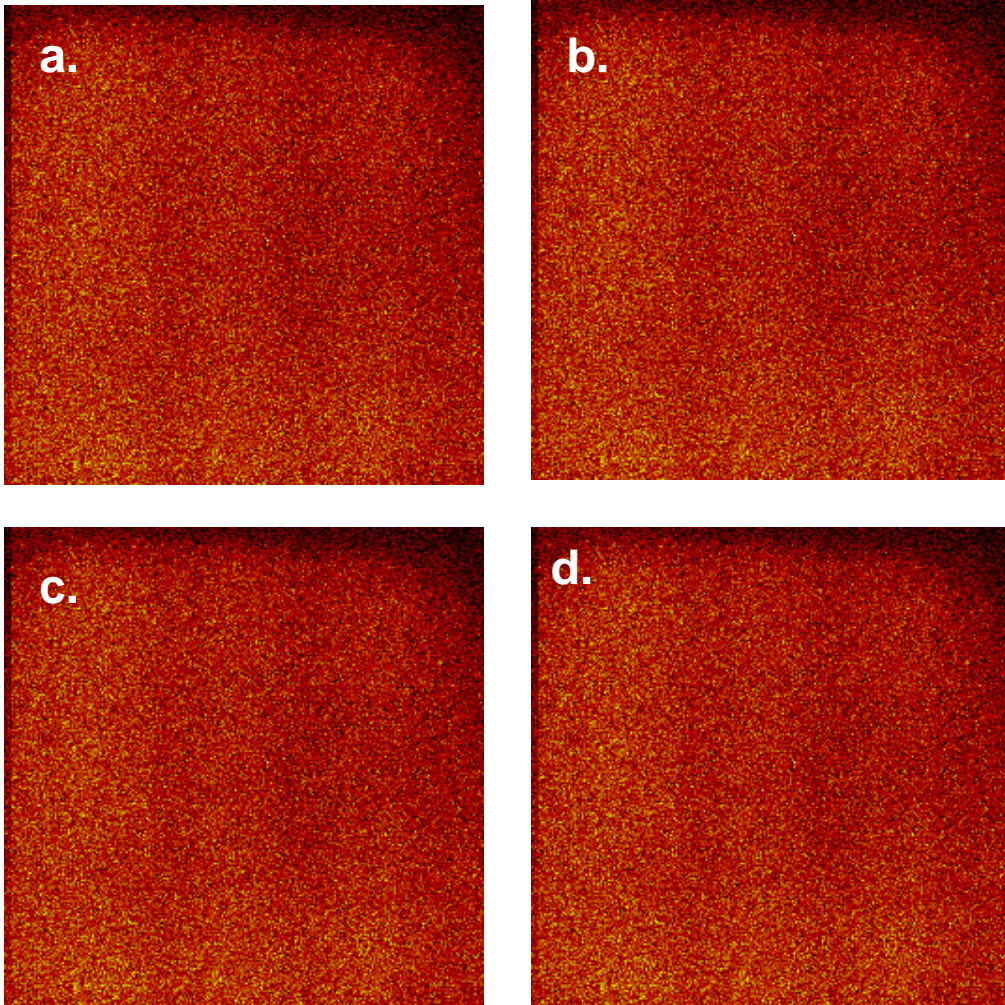


Figure 5.6: TOF-SIMS images of a. Br, b. CH, c. H, d. OH (negative). A 600 pA primary ion current was used over a 200 mm x 200 mm detection area with a 7.2 kV extraction voltage.

Figure 5.7 provides negative ion scanning images of a different region of the PPLN sample. TOF SIMS is a sensitive technique for elemental analysis, which allows the detection of trace impurities. The defect captured shown in 5.7.a. OH and 5.7.d C and absent in the 5.7.b Br image could be indicative of an organic impurity or contamination at the surface.

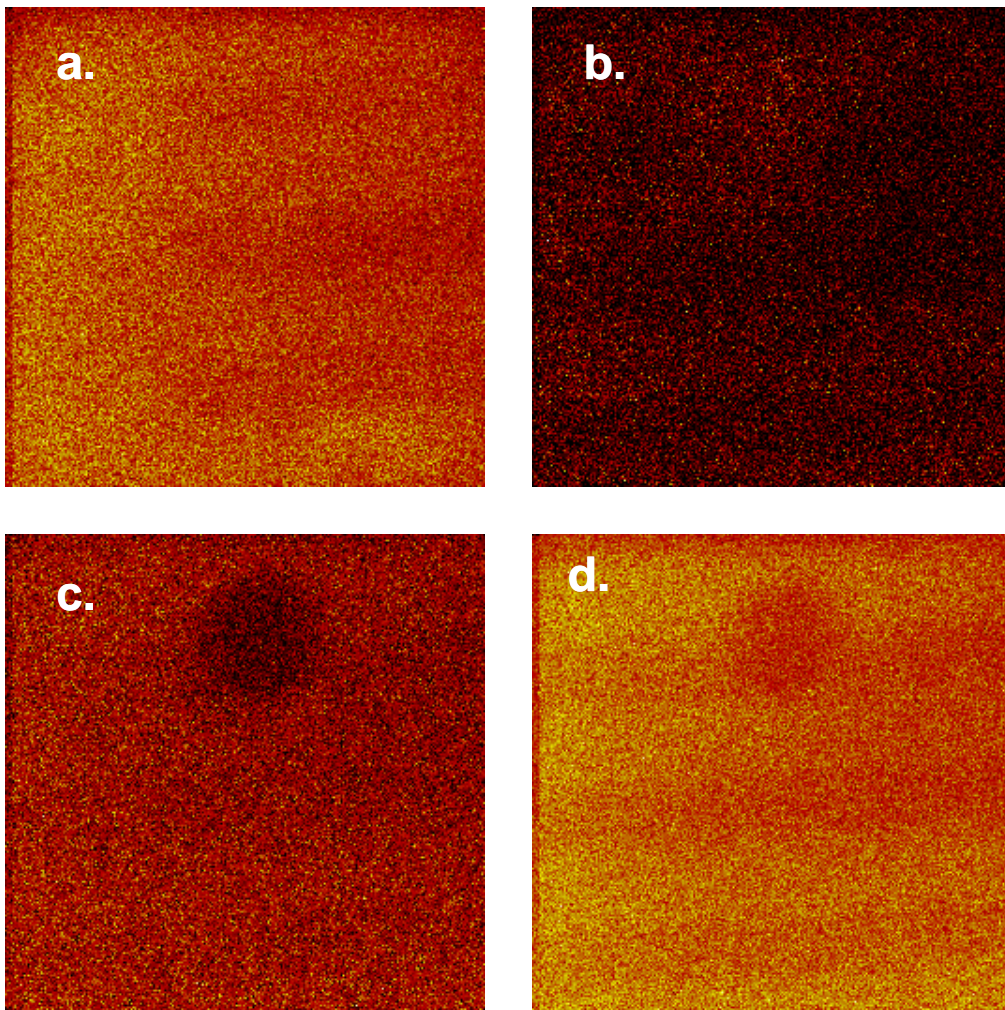


Figure 5.7: TOF-SIMS images of a. H, b. Br, c. OH, d. C (negative). A 600 pA primary ion current was used over a 200 mm x 200 mm detection area with a 7.2 kV extraction voltage.

The embedded contours are still visibly present. We also collected images using positive secondary ions shown in Figure 5.8. Bromine was seen in low yields because of low positive secondary ions detected for the element. From the images in Figures 5.6-8, localization of bromine is not observed.

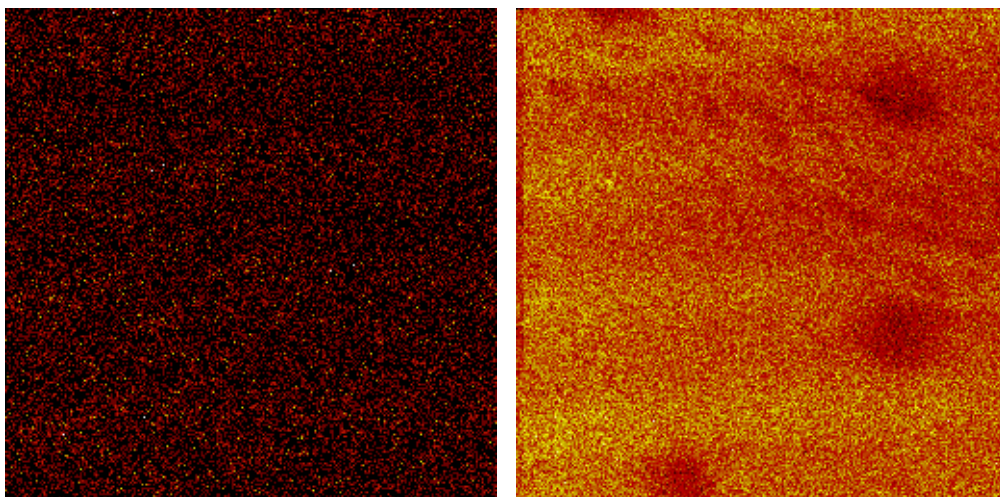


Figure 5.8: TOF-SIMS images of a. Br, b. total scan (positive). A 600 pA primary ion current was used over a 200 mm x 200 mm detection area with a 7.2 kV extraction voltage.

5.4 Conclusions

A method of using self-assembly to develop electrostatic interaction between Bromoacetic acid and poled Lithium Niobate has been reported in this chapter. Here we attempted to demonstrate this phenomenon on two types of poled lithium niobate substrates, a single faced poled surface and periodically poled domains on the surface. We successfully demonstrated selective binding of bromoacetic acid to the single faced poled lithium niobate substrate using XPS. Our results show under specific conditions a 10- fold preference for the positive side of the sample compared to the negative side of the sample could be observed. Selective binding was not observed using periodically poled lithium niobate. The size scale of the poled domain could attribute to the discrepancies in binding. The selective binding was observed on a poled surface of 1 x 1 cm² using XPS versus non-specific binding observed at a 1µm poled region using TOF SIMS. Future work could include Auger Electron

Spectroscopy in addition to XPS. Auger Electron Spectroscopy (AES) provides mobility of the incident electron beam to different regions of a single sample. When used in conjunction with XPS, AES provides mapping of the surface elemental distribution. This spectroscopy instrumentation should be able to detect elements within the μm scale, which would be beneficial in collecting additional information on periodically poled lithium niobate.

5.5 Experimental

5.5.1 Materials

Poled LiNbO_3 substrates were purchased from Crystal Technology, Inc. Single poled LiNbO_3 substrates were purchased .5mm thick, polished on both sides, and z-cut. Chlorotrimethylsilane (TMSCl), dry hexane was obtained from Sigma Aldrich, (St.Louis, MO) and used as received without further purification. All other solvents and chemicals used were of reagent grade.

5.5.2 Surface Passivation

Lithium niobate samples (1 cm x 1cm) were annealed in an ambient furnace at 1000° for two hours. After annealing the substrates cleaning was then followed by water, ethanol rinsing and drying with nitrogen. Delicate handling of only the edge of the sample was very important during the cleaning procedure to avoid compromising the surface charge by contaminating the face of the LiNbO_3 surface.

Silination reactions were then immediately carried out in an enclosed glass chamber. A $30\mu\text{L}$ droplet of Chlorotrimethylsilane (TMSCl) was exposed to each side of the poled

lithium niobate for vapor deposition. Contact angle measurements using a Ramehart optical goniometer were made to ensure even distribution of TMSCl molecules on the lithium niobate surface.

5.5.3 Instrumentation

XPS characterization occurred at pressure of 2×10^{-9} Torr using the 1253.6 eV Mg $K\alpha$ line from a Fisons X3 dual anode source and a Fisons Clam II electron analyzer. The resolution of the analyzer was determined from the full width half maximum of a gold 4f7/2 spectral peak to be approx. 1.0eV, however, through curve fitting, the centroid of spectral peaks can be resolved to ± 0.1 eV. The observation parameters were set to Nb 3d and Br 3d binding energies to record core level shifts.

Surface mapping was performed using time-of-flight (ToF) SIMS with a PHI TRIFT I ToF mass spectrometer. Analysis conditions included 25 keV Ga⁺ primary ion bombardment with detection of positive or negative secondary ions. A 600 pA primary ion current was used over a 200 mm x 200 mm detection area with a 7.2 kV extraction voltage. Charge neutralization was accomplished with a pulsed low energy electron beam (~ 24 eV). Data acquisition time was set to 10min, resulting in a total ion fluency of ca. 5×10^{11} ions/cm² per analysis. Because this is below the so-called static limit, analysis was constrained to the top monolayer (~ 1 nm) of the sample. Both secondary ions were collected from three to four different spots of the sample, secondary ion image were subsequently analyzed using WinCadence software.

5.6 References:

- (1) Kalinin, S.; Alvarez, D.; Lei, T.; Hu, X.; Ferris, Z.; Zhang, Q.; Dunn, S. *Nano Lett.* **2002**, *2*.
- (2) Shrout, T.; Swartz, S. Processing of Ferroelectric and Related Materials: A Review. pp 80-88 in Applications of Ferroelectrics, 1992. Proceedings of the Eighth IEEE International Symposium.
- (3) Alexe, M.; Hesse, D. *Journal of Materials Science* **2006**, *41*, 1-11.
- (4) Purice, A.; Dinescu, G.; Scarisoreanu, N.; Verardi, P.; Craciun, F.; Galassi, C.; Dinsecu, M. *Journal of European Ceramic Society* **2006**, *26*, 2937.
- (5) Auciello, O. *Physics Today* **1998**, *51*, 22.
- (6) Yanagida, H. *Angew, Chem.* **1988**, *100*, 1443.
- (7) Fujimoto, K.; Cho, Y. *Appl. Phys. Lett.* **2003**, *83*, 5265.
- (8) Rosenman, G.; Urenski, P.; Argonin, A.; Rosenaks, Y.; Molotoskii, M. *Appl. Phys. Lett.* **2003**, *82*, 103.
- (9) Bilz, H.; Benedek, G.; Bussmann-Holder, A. *Physical Review B* **1987**, *35*, 4840.
- (10) Kozitskii, Y.; Levitskii, R.; Stasyuk, I. Translated from Teoreticheskaya; Matematcheskaya Fizika, **1979**, *39*, 106
- (11) K. K. Wong, Properties of Lithium Niobate, Data Reviews Series, no. 28, The Institute of Electrical Engineers (London, UK, 2002).
- (12) Kuroda, A.; Kurimura, S.; Uesu, Y. *Appl. Phys. Lett.* **1996**, *69*, 9.
- (13) Yamada, M.; Nada, N.; Sayito, M.; Watanabe, K. *Appl. Phys. Lett.* **1993**, *62*, 435.

(14) Vaidya, R.; Simonson, R.; Cesarano, J.; Dimos, D.; Lopez, G. *Langmuir* **1996**, *12*, 2830-2836.

(15) Moulder, J.; Stickle, W.; Sobol, P.; Bonben, K. *Handbook of Xray Photoelectron Spectroscopy*; Perkin-Elmer Group: Eden Prairie, MN, 1992

Chapter 6: Summary and Outlook

The principal goal of this thesis was centered around surface modification techniques used to enhance potentially useful behavior of material on surfaces. We reported using porous and flat silicon decorated with molecular gradients comprising semifluorinated organosilanes cause an increase in droplet motion. An extension of the droplet motion research was conducted providing a systematic study on the effects of surface tension and viscosity on moving droplets. Modifications were also made to a surface by constructing a polymer brush gradient on silicon to enhance the efficiency in binding and detection of probe molecules. Continuing with the “building up” from the surface technique a poled substrate was also tailored by electrostatically binding polar molecules to form a molecular assembly.

6.1 Systematic Study of Pore Size for Water Motion on Wettability Gradients

In Chapter 2, theoretical analysis has shown that if a high surface tension liquid, such as water, is placed on a porous substrate that is covered with a fluorinated monolayer, the inability of the liquid to wet the pores causes the formation of air pockets inside the pores. Air pockets in turn, lower the friction at the liquid/substrate interface thus increasing the drop velocity. In order to cause friction at the liquid/ substrate interface, electrochemical etching was used to create nanometric sized pores within a silicon substrate While the depth of the pores can be controlled to some degree by the etching time, one typically does not have a good control over the pore sizes and distribution. The difficulties associated with preparing

well-defined pSi substrates can be circumvented by utilizing anodic aluminum oxide (AAO) substrates. AAO with various pore sizes and depths can either be prepared by electrochemical etching of alumina or can be obtained from commercial sources. The use of commercially available AAO is advantageous because it will reduce the sample preparation time. AAO samples can be used as a platform for a systematic study of the of pore size distribution with a controlled density used in droplet motion.

6.2 Movement of liquids containing suspended particles

In Chapters 2 and 3 droplet motion was studied using water and viscous liquids. There are also benefits to conducting research on the movement of liquids containing suspended particles. By successfully distributing particles onto a surface by a liquid medium, new applications in separations can be developed. Research in the area can also lead to distribution of particles in “nano beaker” or “ nano containers within the nanometric sized pores of pSi. However, if the particles remain in the liquid during transport, a method for transporting particles on a gradient surface would be developed. New methods of transporting particle fluids show promise within the fields of nano-manufacturing and directed material synthesis. An investigation of the use of polystyrene spheres as the suspended particle would be beneficial because of the various sphere sizes that are readily available from commercial sources. The novel particle transport procedures on the micro and nano length scales offer reduced sample volumes, assay times, and also procedural costs. Research in this area should address particle/ particle and particle /surface interactions upon liquid movement.

6.3 Systematic study on the Weight Capacity of DNA in a Polymer Brush

In Chapter 4 we identified an efficient method of increasing DNA immobilization and hybridization. A polymer brush molecular weight gradient was used as a platform for DNA attachment. The polymer brush gradient provided chain lengths of various sizes to be studied on a single substrate. Fluorescence microscopy was used to obtain relative fluorescence intensity values indicating DNA hybridization and attachment to the polymer backbone. The microscopy technique provided evidence indicating an increase in DNA attachment to the polymer backbone as the polymer chain length increased. A sequential study of the DNA loading capacity at varying chain lengths will be beneficial in identifying the amount of DNA held within the polymer brush. Quartz Crystal Microscopy would be an ideal technique to use because it involves a mass sensor with capabilities of determining molecular weight changes in the nanogram range. Research detailing the change in weight of dna attached to varying polymer brush chain length scales could lead to quantitative analysis indicating the maximum loading capacity of DNA relative of the chain length.

6.4 Polarization Driven Self-Assembly using Polar Silanes

In Chapter 5 we studied electrostatic interactions between a polarized ferroelectric domain and polar molecules. We successfully demonstrated selective binding of bromoacetic acid to the single faced poled lithium niobate substrate using XPS. An investigation on selective binding of polar silanes such as N- (2-aminoethyl) 3-aminopropyl-trimethoxysilane (AEAPS), will lead to a new, monolayer-based self-assembly strategy on a poled surface. If

the use of polar silanes for selective binding is successful, this technique can be used as a method for creating molecular gradients using SAMs. Molecular gradients using SAMs provide a method of designing a surface with varying chemical interactions along the surface, including wettability. Gradient surfaces are useful in biological and chemical applications, in particular protein adsorption and cell attachment.